Utilizing PET and MALDI Imaging for Discovery of a Targeted Probe for Brain Endocannabinoid *α/β*-Hydrolase Domain 6 (ABHD6)

Karine Mardon[1,2], Jayendra Z. Patel[3], Juha R. Savinainen[4], Damion H. R. Stimson[1], Caitlin R. M. Oyagawa[5], Natasha L. Grimsey[5], Mary-anne Migotto[1], Grace F. M. Njiru[1], Brett R. Hamilton[1,6], Gary Cowin[1,2], Jari Yli-Kauhaluoma[3], Wim Vanduffel[7], Idriss Blakey[1,8,11], Rajiv Bhalla[1], Christopher Cawthorne[9], Sofie Celen[10], Guy Bormans[10], Kristofer J Thurecht[1,8,11,12], Muneer Ahamed[1,8,13]*

muneer.ahamed@sahmri.com

[1]*Centre for Advanced Imaging,*[2]*National Imaging Facility, The University of Queensland, Brisbane 4072, Australia*

[3]*Drug Research Program, Division of Pharmaceutical Chemistry and Technology, Faculty of Pharmacy, University of Helsinki, Viikinkaari 5 E, FI-00014 Helsinki, Finland*

[4]*Institute of Biomedicine, Faculty of Health Sciences, University of Eastern Finland, FI-70211 Kuopio, Finland*

[5]*Department of Pharmacology and Clinical Pharmacology, Centre for Brain Research, and Maurice Wilkins Centre for Molecular Biodiscovery, School of Medical Sciences, Faculty of Medical and Health Sciences, University of Auckland, Auckland 1023, New Zealand*

[6]*Centre for Microscopy and Microanalysis, The University of Queensland, Brisbane 4072, Australia*

[7]*Laboratory for Neuro-and Psychophysiology, Department of Neurosciences, & Leuven Brain Institute, KU Leuven, Leuven, 3000, Belgium*

[8]*ARC Centre for Innovation in Biomedical Imaging Technology, Centre for Advanced Imaging, The University of Queensland, Brisbane 4072, Australia*

[9]*Nuclear Medicine and Molecular Imaging & MoSAIC, Department of Imaging and Pathology, KU Leuven, Leuven 3000, Belgium.*

[10]*Laboratory for Radiopharmaceutical Research, Department of Pharmacy and Pharmacological Sciences, KU Leuven, Leuven 3000, Belgium*

[11]*Australian Institute for Bioengineering and Nanotechnology (AIBN),* [12]*ARC Centre of Excellence in Convergent Bio-Nano Science and Technology (CBNS), The University of Queensland, Brisbane 4072, Australia*

[13]*Molecular Imaging and Therapy Research Unit (MITRU) and National Imaging Facility, South Australian Health and Medical Research Institute (SAHMRI), Adelaide 5000, South Australia (Current Address)*

Abstract Image

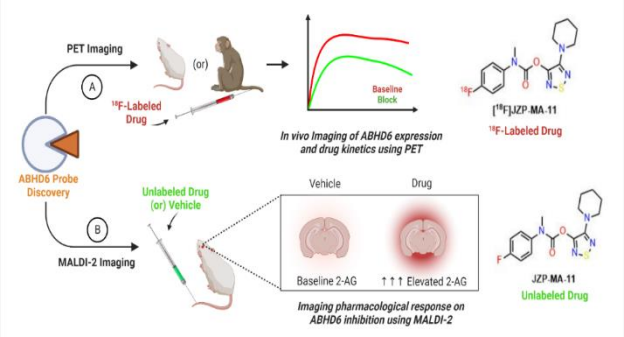

Abstract

Multimodal imaging provides rich biological information, which can be exploited to study drug activity, disease associated phenotypes, and pharmacological responses. Here we show discovery and validation of a new probe targeting the endocannabinoid α/β-hydrolase domain 6 (ABHD6) enzyme by utilizing positron emission tomography (PET) and matrix-assisted laser desorption/ionisation (MALDI) imaging. [^{18}F]JZP-MA-11 as the first PET ligand for in vivo imaging of the ABHD6 is reported and specific uptake in ABHD6-rich peripheral tissues and major brain regions was demonstrated using PET. In vivo pharmacological response upon ABHD6 inhibition was observed by MALDI-2 imaging. A proof-of-concept study in non-human primate confirmed brain uptake. These synergistic imaging efforts used to identify biological information cannot be obtained by a single imaging modality and hold promise for improving the understanding of ABHD6 mediated endocannabinoid metabolism in peripheral and central nervous system disorders.

KEYWORDS: Positron emission tomography, MALDI-2, Endocannabinoids, Brain enzymes, Brain imaging, Fluorine-18, ABHD6.

1. Introduction

Positron emission tomography (PET) is a powerful translational *in vivo* imaging technique used to investigate and diagnose neurological, cardiac and oncological malignancies. Several useful functional parameters can be obtained from PET studies, which can be used to image, stage a disease and also to monitor response to a specific therapy or to investigate expression levels of biomolecules *in vivo* in health and disease. PET imaging has been applied to various components of the endocannabinoid system in the brain and the observed varied expression

levels of enzymes (involved in the synthesis and degradation of the endocannabinoids 2-AG and AEA) in several neurological disorders indicates that these components may be valuable drug targets or biomarker targets.[1–4]

Mass spectroscopy imaging (MSI) offers a route to obtain complementary information by detecting potential aberrations in the diseased tissue microenvironment. Matrix-assisted laser desorption/ionisation (MALDI)-mass spectrometry imaging has emerged as a powerful method for visualising the lipid composition in biological tissues.[5] Integration of MSI with other imaging modalities, particularly with MRI, has been previously demonstrated.[6] The combination of PET and MALDI can be a powerful new step to accelerate the discovery and validation of theranostic probes and rapidly establish pharmacological profiles of new drugs. We set out in this study to image the *in vivo* α/β-hydrolase domain 6 (ABHD6) expression using PET with a new ABHD6 specific radiolabeled probe. Also, we wanted to visualise changes in the expression of the key endocannabinoid lipid 2-arachidonoylglycerol (2-AG) in brain tissues upon pharmacological ABHD6 inhibition using MALDI. For this purpose, we used MALDI post ionisation (MALDI-2) technique, with a trapped ion mobility quadrupole time-of-flight mass spectrometer (timsTOF flex MALDI-2) to image 2-AG expression in brain tissues.

Lipids are an important class of signalling molecules which regulate key biological functions and dysregulation of lipid metabolism underlies chronic pathologies such as cancer, obesity, diabetes, and central nervous system (CNS) disorders.[7] The endocannabinoid 2-AG, is an important signalling lipid in the CNS, which is produced and inactivated by enzymes within the endocannabinoid system (ECS). 2-AG regulates neurotransmitter release in neurons *via* retrograde activation of the presynaptic cannabinoid receptor type 1 (CB_1).[8] 2-AG is also known to act on CB2 receptors (as a full agonist) as an immunomodulator, especially in microglia.[9,10] It is involved in a variety of physiological processes, including modulation of memory, energy balance, and emotional states, such as stress and anxiety.[11]

ABHD6 is a membrane serine hydrolase, and is a secondary enzyme involved in hydrolysis of 2-AG thereby regulating 2-AG signalling in the CNS and peripheral tissues.[12] Other primary enzymes such as monoacylglycerol lipase (MAGL) are known to be responsible for the majority of 2-AG degradation in the brain, however both ABHD6 and MAGL have distinct subcellular and tissue localizations and have distinct roles in regulation of 2-AG. Reverse transcript-PCR analysis indicated high expression of ABHD6 (*m*RNA) in tissues including brain, liver, kidney and ovary.[13] Regional brain distribution indicates that high levels of ABHD6 are found in the frontal cortex, striatum and cerebellum and hippocampal neurons.[14]

Importantly, inhibition of ABHD6 results in only marginal increase of 2-AG in the brain, whereas in contrast pharmacological MAGL inhibition leads to rapid and substantial increase of 2-AG levels in the brain and results in 2-AG dependent CB_1 desensitization.[15] This may indicate ABDH6 inhibition will have potentially less CNS related side effects and less cannabinoid receptor desensitisation.[15,16]

Pharmacological inhibition or genetic deletion of ABHD6 leads to increased levels of 2-AG in the brain and various other tissues, and ABHD6 is involved in many pathophysiological functions, including endocannabinoid signalling, inflammation, insulin secretion and in obesity and metabolic syndromes.[17] Regulation of 2-AG levels *in vivo* in order to produce indirect activation of cannabinoid receptors is an emerging strategy with multiple therapeutic opportunities and thus ABHD6 has been identified as a promising therapeutic target for the treatment of several disorders, particularly in inflammation, metabolic disorders such as obesity, type II diabetes and epilepsy.[18,19] Recently, it was observed that chemical inhibition of ABHD6 showed antiepileptic activity and significantly reduced seizure frequencies in murine models.[20] Interestingly, this was caused by allosterically activating the GABA receptor by increasing endogenous 2-AG levels, *via* a non-cannabinoid (CB_1 and CB_2) mediated mechanism. In peripheral tissues, ABHD6 was found to be the major lipase overexpressed in pancreatic β-cells and is involved in glucose-stimulated insulin secretion *via* a non-endocannabinoid pathway.[21,22] A recent study indicates significant loss in striatal ABHD6 expression in a mouse model of Huntington disease (HD) and also, inhibition of ABHD6 improved motor performance in HD mice.[23] ABHD6 functions as a major MAG lipase in non-small cell lung cancer (NSCLC) and high ABHD6 expression levels were observed in human NSCLC tissues and correlated with advanced tumour node metastasis.[24] All this evidence points to ABHD6 as a potential diagnostic and therapeutic target for multiple CNS and peripheral disorders.

Development of the novel ligands JZP-MA-11 and JZP-MA-13 which show high potency and selectivity for ABHD6 is reported here. Proteome-wide specificity for these compounds were determined using activity-based protein profiling (ABPP) in the mouse brain proteome. Additionally, we show that these compounds do not bind to major endocannabinoid receptors CB_1 and CB_2, and endocannabinoid enzymes MAGL and FAAH. We also report the radiosynthesis of [^{18}F]JZP-MA-11 and the *in vivo* preclinical evaluation of this radiolabelled ligand targeting the brain endocannabinoid degrading enzyme ABHD6 in mice and non-human primate (NHP). To our knowledge, this is the first PET tracer reported for *in vivo* imaging of

ABHD6.[25] Finally, we also show an increased brain 2-AG expression using MALDI-2 imaging in JZP-MA-11-treated mice.

2. Results and Discussions

Patel *et. al.* reported 1,2,5-thiadiazole carbamate-based ABHD6 inhibitors and showed that some of these compounds were potent and highly selective towards ABHD6 when compared to either MAGL, FAAH or ABHD12.[26] We have synthesized two novel compounds JZP-MA-11 (**6a**) and JZP-MA-13 (**6b**) (*Scheme 1*) which contain a thiadiazole carbamate backbone with 4-fluorophenyl substituent, making them suitable as small molecule PET ligands targeting ABHD6. Structures of reference compounds (JZP-MA-11 (**6a**) and JZP-MA-13(**6b**)), PET-precursors (**6c** & **6d**), and their corresponding synthetic routes are shown (*Scheme 1*). Intermediate **5a** was converted to corresponding carbamoyl chloride using triphosgene, which was later coupled with intermediate **4a** or **4b** in presence of base to afford compound **6a** or **6b**. Similarly, intermediate **5b** was converted to corresponding carbamoyl chloride using triphosgene, which was later coupled with either **4a** or **4b** in presence of base to give **6c** and **6d**, respectively.

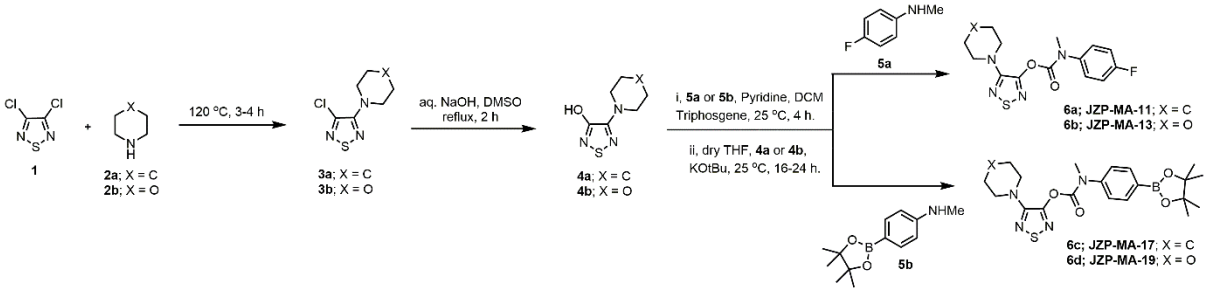

Scheme 1 *Chemical synthesis of reference standards and precursors.*

We have investigated the ability of JZP-MA-11 and JZP-MA-13 (*Figure 1B)* to inhibit human MAGL, ABHD6 and ABHD12, the reported enzymes involved in the degradation of 2-AG. Inhibitory activities against *h*ABHD6 overexpressing HEK-cell lysates and selectivity among mouse metabolic serine hydrolases was determined using whole brain homogenates (C57BL/6JOlaHsd mouse (female, ~2 weeks old)), using the active site serine-targeting fluorescent fluorophosphonate probe (final probe concentration 2 μM), (carboxytetramethylrhodamine fluorophosphonate, TAMRA-FP) as previously described.[27] Based on screening of inhibition profiles for these inhibitors with competitive ABPP (*Figure 1A*), JZP-MA-11 was found to inhibit mouse brain ABHD6 at a concentration of 100 nM and

was fully effective at 1 µM concentration. JZP-MA-13 appeared slightly less potent but was selective for ABHD6 among the enzymes tested (no inhibition of MAGL, ABHD12, FAAH or other serine hydrolases). The good potency and selectivity of these inhibitors for ABHD6 over MAGL and ABHD12 were verified for the corresponding human enzymes (*Figures 1C* and *D*). Further, monitoring glycerol production (end-product of 2-AG hydrolysis) in HEK293 cell lysates using individually overexpressing *h*MAGL, *h*ABHD6 and *h*ABHD12 demonstrated ABHD6 selectivity of both compounds among these three enzymes known to be involved in 2-AG hydrolysis. Both inhibitors were practically silent against human MAGL and ABHD12 (*Figure 1D*) but were potent in inhibiting ABHD6 with IC_{50}-values of 126 (±22) nM (JZP-MA-11) and 392 (±77) nM (JZP-MA-13). To explore inhibitor selectivity and activity more closely in mouse tissues, we examined competitive ABPP in mouse (C57BL/6JOlaHsd mouse (female, ~2 weeks old)) heart, liver and kidney homogenates (*Figure S1*). These experiments revealed that mouse ABHD6 has relatively low activity in these tissues compared to that found in the brain tissue (*Figure 1*), as previously observed.[28] Interestingly, neither JZP-MA-11 nor JZP-MA-13 show any off-target activity at 100 nM. However, at higher concentration (1 µM), JZP-MA-11 and JZP-MA-13 inhibited an additional serine hydrolase (or several unidentified ones with similar molecular weight, ~63 kDa), most likely representing FAAH based on the reference inhibitor activity (JZP-327A).[29]

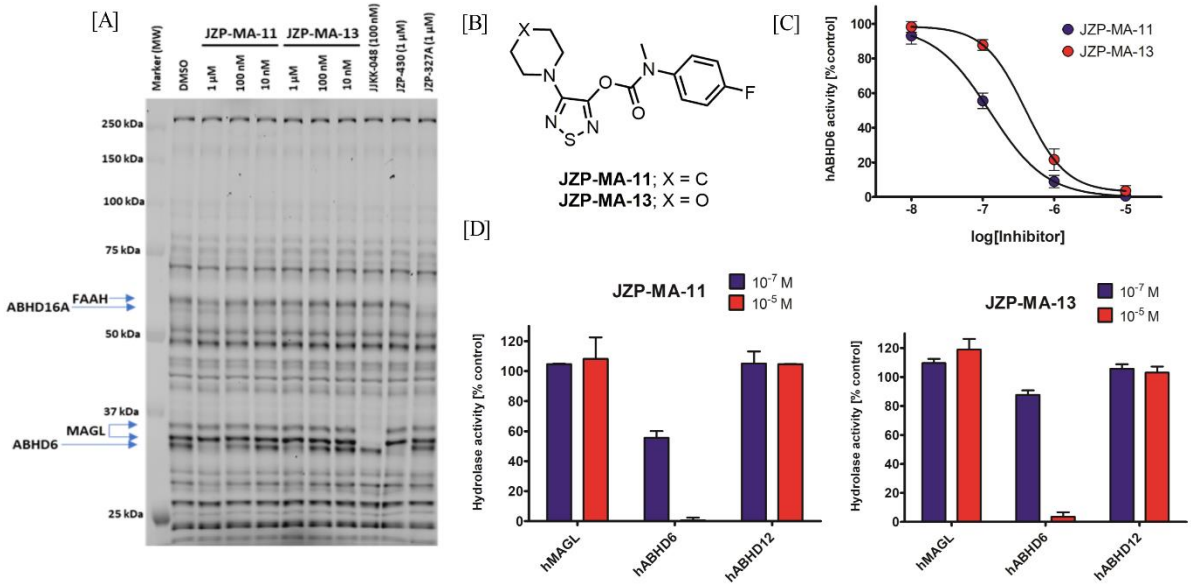

Figure 1. JZP-MA-11 and JZP-MA-13 show high selectivity for ABHD6 in mouse whole-brain proteome assessed by competitive ABPP and low nano-molar activity in glycerol-based enzymatic assay. *The chemical structures (panel* ***B****) and selectivity of compounds JZP-MA-11 and JZP-MA-13 to inhibit ABHD6 among the serine hydrolases in mouse whole-brain proteome by competitive ABPP*

*(panel **A**) is shown. The result is a representative of three ABPP experiments with similar outcomes. Molecular weight markers are indicated at left, in addition to protein bands corresponding to ABHD6, MAGL (doublet), ABHD12 as well as for FAAH and ABHD16A. Reference inhibitors JJKK-048*[30]*, JZP-430*[26] *and JZP-327A*[29] *were used at the indicated concentrations to identify the serine hydrolases MAGL, ABHD6 and FAAH, respectively. The potency to inhibit human ABHD6 **(C)** and selectivity over human MAGL and ABHD12 **(D)** were tested by the glycerol-based assay.*

Next, we wanted to rule out any functional agonism or antagonism of our lead compounds towards the two major cannabinoid receptors (CB1 and CB2). CB_1 and CB_2 canonically couple to $G\alpha_{i/o}$ proteins, which on activation result in inhibition of adenylyl cyclase and reduction in intracellular cAMP.[31] To determine whether JZP-MA-11 and JZP-MA-13 influence canonical CB_1 or CB_2 signalling, we investigated their effects on forskolin-stimulated cAMP using a real-time CAMYEL cAMP biosensor assay.[32] CP 55,940 (a full agonist at both CB_1 and CB_2), SR141716A (CB_1-selective inverse agonist), and SR144528 (CB_2-selective inverse agonist) were included for comparative reference and also co-incubated with the ABHD6 inhibitors so as to detect potential competitive or allosteric interaction. As expected[33–35], CP 55,940 inhibited forskolin-stimulated cAMP by ~50% at CB_1, and ~40% at CB_2, and inverse agonists SR141716A and SR144528 increased forskolin-stimulated cAMP by ~20% at CB_1, and ~50% at CB_2, respectively *(Figure 2)*. In contrast, neither JZP-MA-11 nor JZP-MA-13 (10 µM) had an effect on forskolin-stimulated cAMP in cells expressing CB_1 or CB_2 *(Figure 2)*, suggesting that these compounds do not act as direct agonists or inverse agonists at either receptor. The co-application of JZP-MA-11 or JZP-MA-13 did not modify any of the orthosteric ligand responses, indicating that these compounds are not acting as neutral antagonists, nor allosteric modulators, at either CB_1 or CB_2. These data indicates that neither JZP-MA-11 nor JZP-MA-13 binds orthosterically to CB_1 or CB_2 or allosterically influences canonical CB_1 or CB_2 signalling.

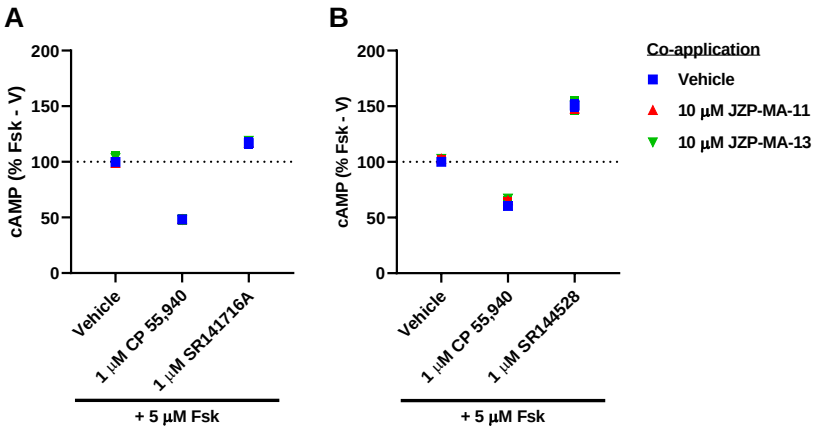

C

	hABDH6	*hABDH12*	*hMAGL*	*hCB$_1$*	*hCB$_2$*	*cLogP*	*MW*	*TPSA*
JZP-MA-11	126±22 nM	>10 µM	>10 µM	na	na	3.01	336.36	86.8
JZP-MA-13	392±77 nM	>10 µM	>10 µM	na	na	2.15	338.36	96.0

Figure 2. JZP-MA-11 and JZP-MA-13 do not influence CB$_1$/CB$_2$ cAMP signalling. *HEK293 cells stably expressing* ***(A)*** *hCB$_1$ or* ***(B)*** *hCB$_2$ were stimulated with 5 µM forskolin and vehicle or 1 µM CP 55,940, SR141716A (CB$_1$), or SR144528 (CB$_2$), in the absence or presence of 10 µM JZP-MA-11 or JZP-MA-13. Data were normalised to cells treated with vehicle alone (V; 0%) and forskolin alone (Fsk; 100%), and are presented as mean ± SEM from three independent experiments.* ***(C)*** *Table summarizing key parameters for JZP-MA-11 and JZP-MA-13 (na = no activity detected at 10 µM). Values for ABHD6-, ABHD12- and MAGL-inhibition are from the glycerol assay (SEM, n=3-5 independent experiments). Additionally, cLogP (Calculated partition coefficient), MW (Molecular weight) and cTPSA (Calculated total polar surface area) were calculated using the SwissADME online suite.*[36]

JZP-MA-11 was selected for further radiotracer development based on our promising pharmacological data, which points at high potency and selectivity for ABHD6. Also, no inhibition for MAGL or ABHD12 and no off-target activity was detected in the brain proteome and no CB1 and CB2 agonism or antagonism was detected at 10 µM *(Table 2C)*. Given the recent advancement in new ^{18}F-aromatic fluorination methodologies, radiosynthesis of [^{18}F]JZP-MA-11 can be suitably carried out *via* copper-mediated aromatic nucleophilic ^{18}F-fluorination. Copper-mediated aromatic nucleophilic ^{18}F-fluorination is an attractive methodology to generate useful ^{18}F-PET ligands in the final step of radiosynthesis, which otherwise would be difficult to obtain using traditional [^{18}F]-fluorination methods. This method typically involves the use of aryl boronic esters, aryl boronic acids or aryl stannanes as precursors and is mediated by copper salts. In the last decade both metal-mediated and metal-free nucleophilic [^{18}F]-fluorination reactions were reported employing various aryl-precursors.

For example, the scope of the aryl precursors ranges from using iodonium salts[37], iodonium ylides[38], sulfonium salts[39,40] boronate esters[41] to the, recently using aryl halides[42]. Among these, the copper-mediated direct ^{18}F-fluorination of arylboronate esters[43] and arylboronic acids[44] are commonly used. Improvements such as metal-free approaches have also been reported[37,38], however easy access to boronate esters has facilitated the late-stage one-step labelling of aromatics *via* copper-mediated ^{18}F-fluorination of arenes and is finding widespread application.

The automated radio synthesis of [^{18}F]JZP-MA-11 starting from the corresponding boronate ester precursor (JZP-MA-17) using a copper-mediated fluorination on a Synthra RN plus platform was adopted as previously reported.[45–47] Briefly, JZP-MA-17 and $[Cu(Py)_4](OTf)_2$ in anhydrous DMA was reacted with dried [^{18}F]Et_4NF. The reaction was carried out at 110 °C for 20 min, followed by HPLC purification and reformulation using a C18 SPE to yield [^{18}F]JZP-MA-11 (*Scheme S2*). The overall automated synthesis time was approximately 71 min, including purification and formulation. [^{18}F]JZP-MA-11 was obtained with a high radiochemical purity of >99% (n=9), and a molar activity of 180±110 GBq/µmol (n=9). The radiochemical yield was low 3.2% ± 0.8 (n=9), however sufficient for pre-clinical evaluation in small animals and non-human primates (NHP) *(Figure 3)*. Stability of [^{18}F]JZP-MA-11 indicated about 97% of intact tracer at 210 min post production, indicating that [^{18}F]JZP-MA-11 was sufficiently stable in the formulation (*Scheme S3*).

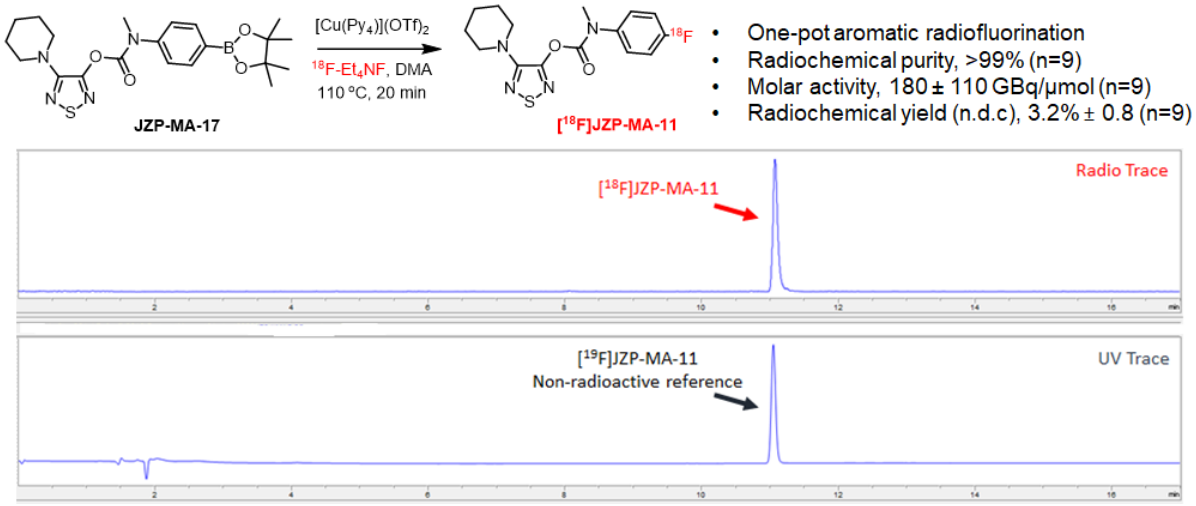

Figure 3. Radiosynthesis of [^{18}F]JZP-MA-11 using copper-mediated ^{18}F-aromatic fluorination. *Purity and identity of [^{18}F]JZP-MA-11. Retention times of non radioactive reference JZP-MA-11 (UV channel) and [^{18}F]JZP-MA-11 (radio channel) were identical, [^{18}F]JZP-MA-11 was co-injected with reference JZP-MA-11.*

In order to evaluate the suitability of [^{18}F]JZP-MA-11 for *in vivo* mapping of ABHD6, kinetics and binding properties were verified using dynamic PET/CT acquisitions in healthy C57BL6 mice (female, 10-12-week -old) (*Figure 4). In vivo* PET/CT images showed the tracer readily crossed the blood-brain barrier (BBB) and the corresponding time–activity curves (TAC) for the whole brain are shown in *Figure 4A.* [^{18}F]JZP-MA-11 showed high initial brain uptake (~1.5 SUV or ~9.1% ID/g at 2.2 min p.i.), followed by plateaued TACs (*Figure 4A).* No significant washout from the whole brain was observed during the 60-min baseline PET scan, as the ratio of $SUV_{2.5}/SUV_{60\ min}$ remained high at 3.5 and the average $SUV_{5\text{-}60\ min}$ was ~0.5. This is indicative of typical irreversible binding kinetics, representative irreversible PET ligands from literature for imaging MAGL showed similar binding profile in the brain.[48,49] Also, in recent past enormous efforts have been made for the discovery and development of irreversible PET ligands targeting hydrolases enzyme-based biomarkers for diagnosis and several of them show similar kinetics. It should be noted that no uptake in bone was observed for [^{18}F]JZP-MA-11, indicating absence of *in vivo* defluorination of the tracer. *In vivo* PET-MR imaging in healthy Sprague-Dawley rats (male, 10-12-week-old) indicated that the brain uptake profile was similar to healthy C57BL6 mice, with homogenous distribution of the tracer in different rat brain regions (*Figure 4F & S4*). It also has to be noted that the rat brain uptake was slightly higher than mice (average $SUV_{17\text{-}60\ min}$: 0.57 vs 0.43).

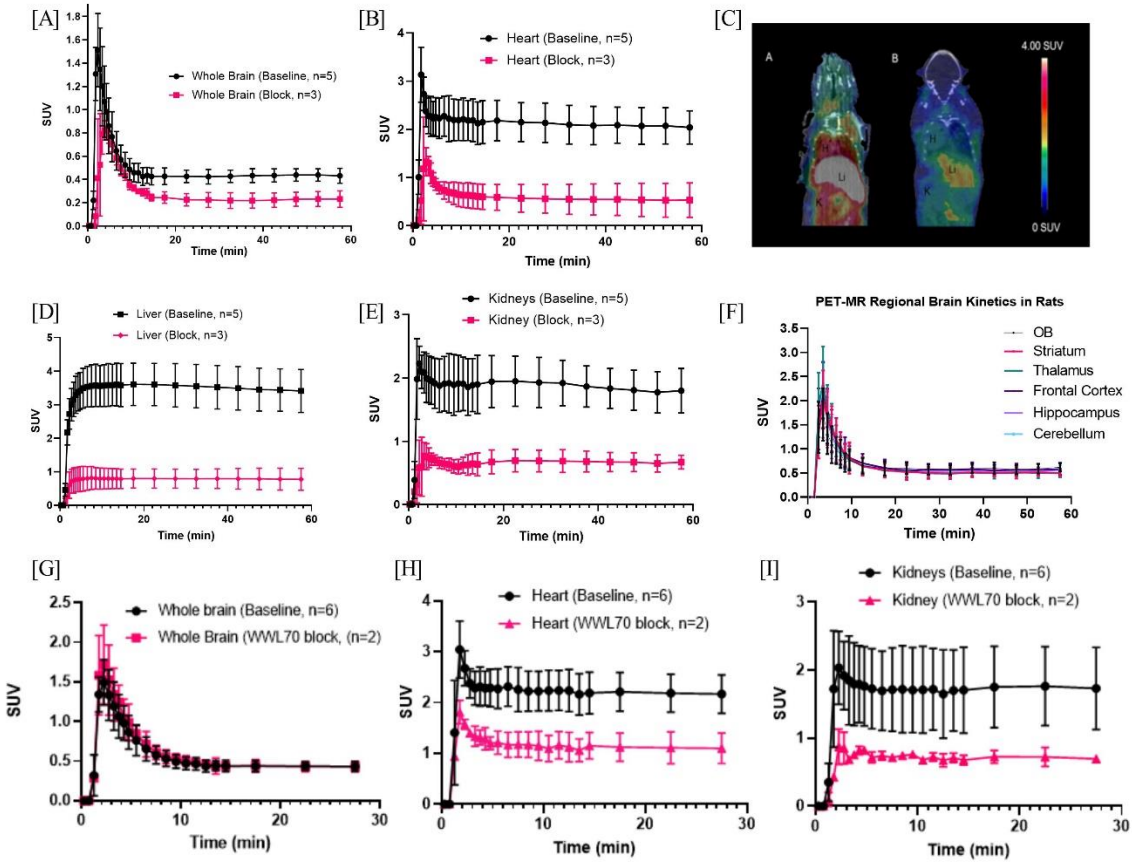

Figure 4. [^{18}F]JZP-MA-11 shows ABHD6 specific uptake in vivo. *In vivo tracer kinetics for the whole organ under baseline conditions after i.v. injection of [^{18}F]JZP-MA-11 and corresponding kinetics after blocking with JZP-MA-11 (1.5 mg/kg; iv) 20 min before tracer injection in* healthy *C57BL6 mice (female, 10-12-week-old) under gaseous anesthesia [**A**,**B** & **D**,**E**]. Representative averaged summed (30-60 min) PET/CT images (horizontal section) showing organs uptake (H, heart; Li, Liver and K, Kidney) from two animals: baseline (left), after blocking with JZP-MA-11, i.v 20 min before tracer injection (right) [**C**]. Time activity curves (TAC) of major brain regions in healthy Sprague-Dawley rats (male, 10-12-week-old), generated using simultaneous PET/MRI after injection of [^{18}F]JZP-MA-11 under baseline conditions [**F**]. In vivo tracer kinetics after blocking with WWL70 (0.75 mg/kg) 45 min before tracer injection in healthy C57BL6 mice (female, 10-12-week-old) [**G-I**].*

Our baseline experiments indicated high uptake and retention in ABHD6 rich tissues such as liver, heart and kidneys (*Figure 4B,D&E*), which are known to have high *m*RNA expression of ABHD6.[50] Excretion of the tracer was observed to be predominantly *via* renal pathways, as seen by increasing accumulation in the bladder from the kidneys *(Scheme S5).* To verify ABHD6 specific uptake in various organs of interest, we performed a competition blocking experiment with JZP-MA-11 (non-radioactive reference). Pretreatment with JZP-MA-11 (1.5

mg/kg, 20 min before tracer, *iv*) resulted in a decrease in radioactivity uptake in ABHD6-rich organs such as, brain, liver, heart and kidneys *(Figure 4A-F)*. Blocking effects (average $SUV_{17\text{-}60\ min}$) were observed in the heart (73%), liver (77%) and kidneys (63%) indicating ABHD6 specific binding in these organs *(Scheme S5)*. Whole brain uptake could also be blocked (47% decrease) and suggests ABHD6 specific uptake in the healthy brain. This *in vivo* ABHD6 specific brain uptake is in accordance with our ABPP experiments performed in the mouse brain proteome *(Figure 1A)*. To further investigate ABHD6 selective binding, a blocking study with a structurally non-related ABHD6 inhibitor (WWL70, 0.75 mg/kg) was administered 45 min before tracer. In heart and kidneys, the accumulation of the radioactivity was reduced when compared to baseline, indicating ABHD6 selective uptake *(Figure 4G-I)*. In the healthy female C57BL6 mouse brain, however the TAC of baseline and block overlapped and a blocking effect was not observed. However, such effects for neuro-PET ligands are not uncommon and have been attributed to increased plasma concentration of tracer due to peripheral blocking effects and (or) blood flow changes.[51,52] Another possible reason could be the limited brain uptake of WWL70 compared to JZP-MA-11.

Next we performed an *ex vivo* experiment to determine the extent of irreversible binding of [^{18}F]JZP-MA-11 in healthy C57BL6 mice (female, 10-12-week-old) brain homogenate. Following *i.v.* injection of [^{18}F]JZP-MA-11 in mice (n=3), the animals were sacrificied at 30 min after injection to obtain homogenised brain tissue. The amount of tracer irreversibly bound was determined by measuring the radioactivity in the pellet and extracts. The extraction efficiency of [^{18}F]JZP-MA-11 from brain tissue was low (10.1±3.0%), indicating that about 90% of the radioactivity was irreversibly bound to the brain tissue at 30 min post injection. These results confirm the irreversible binding of [^{18}F]JZP-MA-11 in the brain and further supports the *in vivo* brain kinetics results (*Figure 4A)*. We have also investigated the metabolites of unbound radioactivity in healthy C57BL6 mouse (female, 10-12-week-old) brain, plasma, kidneys, liver and heart at 30 min post tracer injection (n=2), using both reverse and normal phase TLC analysis. Normal and reverse phase TLC analysis of the brain indicated about 22% and 15% of intact [^{18}F]JZP-MA-11 in the extractable fraction respectively, showing two major polar metabolites at 30 min *(Scheme S5)*.

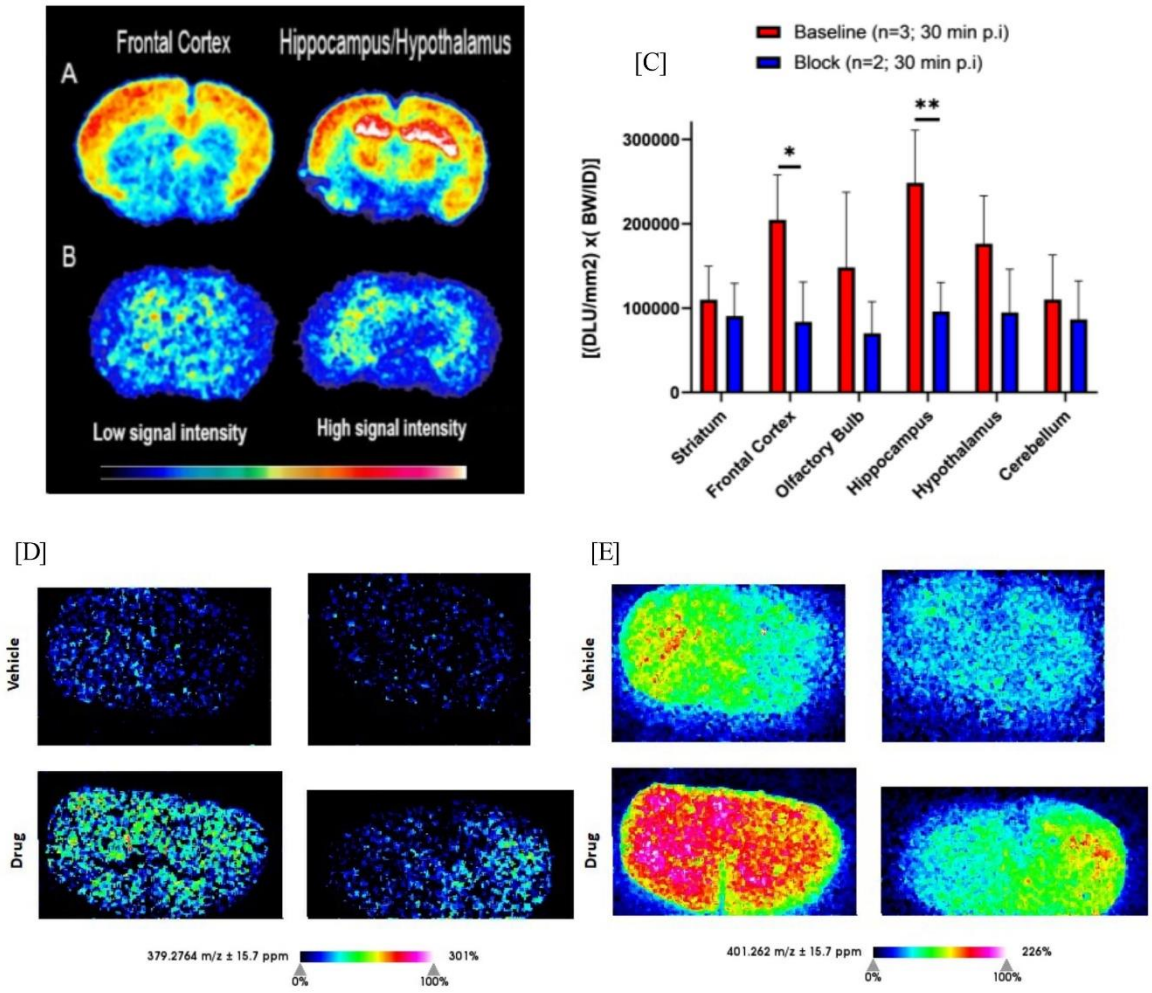

Figure 5. High resolution ex vivo autoradiography and MALDI-2 imaging. *Representative autoradiograms of healthy C57BL6 mouse brain tissues (female, 10-12-week-old) after injection of [^{18}F]JZP-MA-11. [**A**] Total tracer binding to brain was determined 30 min after injection of [^{18}F]JZP-MA-11 (n=3). [**B**] Non-specific binding was determined 30 min after injection of [^{18}F]JZP-MA-11, under blocking conditions with JZP-MA-11 (1.5 mg/kg, iv, 20 min prior to tracer injection, n=2). [**C**] Corresponding autoradiogram data quantification using ImageQuant. The results are expressed as digital light units per square millimeter normalized for body weight of the animal and injected dose [(DLU/mm2) × (body weight/injected dose)] and asterisks indicate statistical significance * = $P \leq 0.05$, ** = $P \leq 0.01$. [**D&E**] Imaging pharmacological response using the state-of-the-art MALDI-2 imaging. MALDI-2 IMS ion images showing the distribution of 2-AG in the healthy C57BL6 mouse brain (two non-adjecent brain tissues) treated with vehicle or drug (JZP-MA-11, 1.0 mg/kg, 30 min prior to sacrifice, n=2). Images for (**D**) m/z 379.27 $[M+H]^+$ and (**E**) m/z 401.26 $[M+Na]^+$ are shown. Intensities of extracted ions (±1 Da) from normalized spectra are shown as heat maps across the tissue section.*

Evaluation of ABHD6 in specific brain regions is of particular interest, because as previous reports indicate that enzymes which regulate endocannabinoid levels have significant variation in activity levels in different brain regions resulting in regionally dependent CNS lipid signalling and neurotransmission.[14,53] We therefore proceeded to analyse regional brain uptake of [^{18}F]JZP-MA-11 using high resolution autoradiography imaging. *In vitro* autoradiography experiments were performed on healthy C57BL6 mouse brain slices (female, 10-12-week-old) to assess the specificity of binding (n=5-7) (*Figure S7*). Slices were incubated with [^{18}F]JZP-MA-11 in the presence of [^{19}F]JZP-MA-11 and the structurally non-related ABHD6 inhibitor WWL70[54]. Whole brain uptake could be blocked up to 92% using [^{19}F]JZP-MA-11 (20 µM) and a dose dependent blocking of 55%, 31% and 13% was observed using 100, 50 and 10 µM of WWL70 respectively (n=5-7). Tracer uptake was highest in amygdala, frontal cortex, hippocampus and olfactory bulb, and the uptake in these regions could be blocked using [^{19}F]JZP-MA-11 (20 µM). Further a dose dependent blocking of the tracer binding was observed in frontal cortex (55%, 40% and 8%) and olfactory bulb (52%, 26% and 3%) using 100, 50 and 10 µM of WWL70 (*Figure S7*).

For *ex vivo* autoradiography performed 30 min post tracer injection, we used healthy C57BL6 mice (female, 10-12-week-old both control mice (n=3) and mice pretreated with JZP-MA-11 (n=2, 1.5 mg/kg) to determine *ex vivo* specific binding of [^{18}F]JZP-MA-11 in major brain regions (*Figure 5A-C*). [^{18}F]JZP-MA-11 was injected in healthy female C57BL6 mice (n=3) and animals were sacrificed (30 min p.i) to remove brain. For the competition study, animals were treated with [^{19}F]JZP-MA-11, 20 min before tracer injection followed by sacrificing the animals to extract brain slices (30 min p.i of [^{18}F]JZP-MA-11). Under baseline conditions, [^{18}F]JZP-MA-11 showed high uptake in distinct brain regions, such as hippocampus, frontal cortex, striatum, hypothalamus and olfactory bulb. Also, pretreatment exhibited a high degree of specific binding as reduced uptake in regional brain regions as compared to baseline conditions (*Figure 5A&B*). For example, we observed a blocking effect of 61%, 59%, 46% and 53% in hippocampus, frontal cortex, hypothalamus and olfactory bulb respectively, demonstrating high specificity of binding of [^{18}F]JZP-MA-11 in brain (*Figure 5C*). These results demonstrated the high selectivity of [^{18}F]JZP-MA-11 toward brain ABHD6 in specific brain regions. Furthermore, the observed regional brain uptake of [^{18}F]JZP-MA-11 using *ex vivo* autoradiography is consistent with mouse immunohistochemical expression patterns of ABHD6 reported in open source Allen brain atlas project (*Figure S8*).[55]

Further validation of JZP-MA-11 was carried out using Mass Spectrometry Imaging (MSI) utilising a Bruker tims TOF Flex equipped with MALDI-2, to specifically image lipid level

changes as a pharmacological response on ABHD6 inhibition using JZP-MA-11 (*Figure 5D&E*). Inhibiting endocannabinoid degrading enzymes like MAGL or ABHD6 results in an increase in 2-AG in the brain pool. To image 2-AG in healthy C57BL6 mouse brain tissues (female, 10-12-week-old), animals were treated either with vehicle or JZP-MA-11 (i.v., 1.0 mg/kg) to see the varied distribution of 2-AG. We could image 2-AG at detectable levels as its parent ion as well as its sodium adduct (*m/z* 379.277 and *m/z* 401.259, respectively) in the drug treated mouse tissue, although at a very low signal intensity and relatively homogenous within the brain slice. Relatively, in vehicle treated animals the amount of 2-AG was found to be qualitatively low when compared to drug treated animals (*Figure 5D&E*). The 2-AG ion signal was found in a very small m/z window and disappeared upon a small mass change, hence we believe the signal was with very high probability related to 2-AG (or an isomer) and not from any background signal.

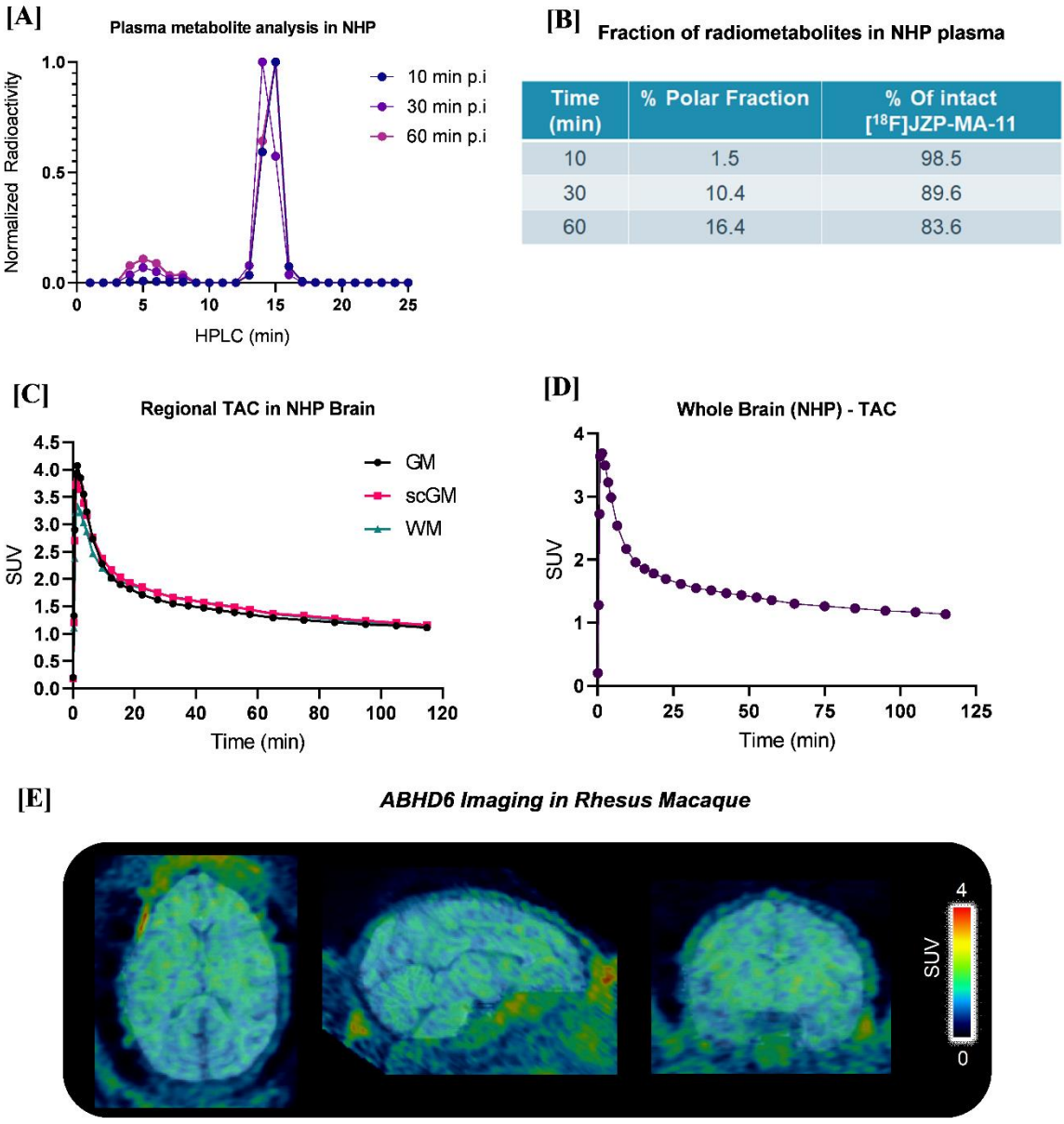

Time (min)	% Polar Fraction	% Of intact [^{18}F]JZP-MA-11
10	1.5	98.5
30	10.4	89.6
60	16.4	83.6

Figure 6. PET/MR imaging of ABHD6 in NHP *(Macaca mulatta, n=1, 10.4 kg).* ***[A&B]*** *Fraction of radiometabolites in NHP venous plasma of [^{18}F]JZP-MA-11 at 10, 30 and 60 min.* ***[C]*** *Baseline time activity curves for grey matter (GM), white matter (WM) and sub-cortical grey matter (scGM) in NHP brain.* ***[D]*** *Baseline time activity curve in NHP whole brain.* ***[E]*** *Coronal, Sagittal and Transaxial (left to right) NHP brain summed PET images between 30-120 min post-injection.*

For potential clinical translation of [^{18}F]JZP-MA-11, we carried out a proof-of-concept imaging study in a NHP.

The fraction of radiometabolites was determined in venous monkey plasma at 10, 30 and 60 min post tracer injection (n=1 for each time point) using HPLC. At 10 min post tracer injection, 99% of the recovered radioactivity in plasma was in the form of intact tracer. At 30 and 60

min, this was still 90% and 84%, respectively (*Figure 6A&6B*). Only polar radiometabolites (relative to the intact tracer) were detected and the recovery of the activity from HPLC was 94% (n = 3). PET imaging in NHP indicated that [^{18}F]JZP-MA-11 readily crossed the blood-brain-barrier and the tracer uptake decreased during the 120 min scan (*Figure 6D&6E*). The regional brain distribution of [^{18}F]JZP-MA-11 was homogenous between grey and white matter (*Figure 6C*).

3. Conclusions

We combined the complementary information gained through PET and MALDI-2 imaging for the discovery and validation of a new highly selective probe targeting the endocannabinoid ABHD6. The *in vivo* mapping of ABHD6 in mice, rats and NHP by PET and *ex vivo* MALDI-2 imaging of a pharmacological response offers a unique approach for improved understanding of ABHD6 mediated disorders. These synergistic imaging efforts hold promise for accelerating drug and theranostics discovery of ligands targeting complex enzyme signatures and lipid metabolism. Moreover, these image-based features can be collectively used to identify biological information, correlating observations and conclusions made from *in vivo* and *ex vivo* molecular imaging techniques.

In the mouse brain proteome, JZP-MA-11 displayed high selectivity for ABHD6 among the other brain serine hydrolases and also no functional agonism or antagonism was detected for the two major cannabinoid receptors (CB1 and CB2). Utilisation of copper-mediated ^{18}F-aromatic fluorination enabled radiosynthesis of [^{18}F]JZP-MA-11 suitable for *in vivo* PET imaging. *In vivo* imaging experiments indicated ABHD6-specific uptake in brain and other peripheral organs, indicating potential applications in both ABHD6-mediated CNS and non-CNS related theranostics. Furthermore, high resolution *ex vivo* autoradiography imaging indicated high and blockable brain tracer uptake, especially high displacement was seen in the cortex, olfactory bulb and hippocampus, indicating ABHD6 specific binding in these brain regions. To our knowledge, this is also the first potent and highly specific PET radioligand for the endocannabinoid hydrolysing enzyme ABHD6. MALDI-2 imaging showed elevated 2-AG levels in brain tissues of JZP-MA-11 treated animals. Finally, proof-of-concept PET imaging studies in NHP confirmed brain uptake and indicated a low fraction of radiometabolites in venous plasma after injection of [^{18}F]JZP-MA-11. Further detailed investigations are warranted in ABHD6 knock-out animals and other preclinical models to assess the suitability of [^{18}F]JZP-

MA-11 for direct assessment of disease and relevant drugs on the ABHD6 activity *in vivo* and to assess the suitability of [^{18}F]JZP-MA-11 as a lead tracer for first-in-human studies.

4. Experimental Section

Reagents and solvents used were purchased from commercial suppliers, such as Sigma-Aldrich (Germany) and Fluorochem (United Kingdom) and were used without further purification. Moisture-sensitive reactions were conducted using dry solvents in an inert atmosphere of dry argon. Most of the reactions were monitored by thin-layer chromatography (TLC) using aluminum sheets coated with silica gel F_{245} (60 Å, 40-63 μm, 230-400 mesh, Merck, Darmstadt, Germany) with suitable UV visualization (254/366 nm). ^{1}H-NMR and ^{13}C- NMR spectra were recorded on a Bruker Ascend 400 MHz—Avance III HD NMR spectrometer (Bruker Corporation, Billerica, MA, USA) (^{1}H at 400 MHz and ^{13}C at 100 MHz) at ambient temperature. Tetramethylsilane (TMS) was used as an internal standard for ^{1}H-NMR. Chemical shifts are reported in parts per million and referenced indirectly to TMS *via* the residual solvent signals (^{1}H, $CDCl_3$ at 7.26 ppm, or DMSO-d_6 at 2.50 ppm; ^{13}C, $CDCl_3$ at 77.16 ppm, or DMSO-d_6 at 39.52 ppm). All spectra were processed for recorded FID files with MestReNova 11.0.4 software (Mestrelab Research, Santiago de Compostela, Spain). The following abbreviations are used: s, singlet; d, doublet; m, multiplet; dd, double of doublet; br s, broad singlet. Low resolution mass (MS-APCI) analyses were performed on a MS Advion expression® CMS spectrometer equipped with an APCI ion source and an Atmospheric Solids Analysis Probe (ASAP) and the data was reported for the molecular ions $[M+H]^+$. Exact mass and purity (>97%) of all tested compounds was confirmed by LC-MS analyses with a Waters Acquity® UPLC system (Waters, Milford, MA, USA) equipped with an Acquity UPLC® BEH C18 column (1.7 μm, 50 mm × 2.1 mm, Waters, Ireland), an Acquity PDA detector and a Waters Synapt G2 HDMS mass spectrometer (Waters, Milford, MA, USA) *via* an ESI ion source in positive mode. High resolution mass (HRMS-ESI) data was reported for the molecular ions $[M+H]^+$.

4.1. Chemistry and Synthesis

Synthesis of ABHD6 reference compounds (6a & 6b) and PET-precursors (6c & 6d)

Reference compounds (**6a** & **6b**) and PET-precursors (**6c** & **6d**) were synthesized as previously reported.[26]

4-(Piperidin-1-yl)-1,2,5-thiadiazol-3-yl (4-fluorophenyl)(methyl)carbamate (JZP-MA-11, **6a**)

White solid (0.19 g, 26%); ^{1}H-NMR (400 MHz, $CDCl_3$): δ 7.23 (dd, J = 8.6, 4.7 Hz, 2H), 7.07-6.99 (m, 2H), 3.31 (s, 4H), 3.11 (s, 3H), 1.64 (s, 6H); ^{13}C-NMR (101 MHz, $CDCl_3$): δ 163.01, 160.53, 153.56, 151.08, 146.26, 138.16, 128.51, 116.57, 116.34, 49.08 (2C), 39.05, 25.51 (2C), 24.23; ESI-MS (*m/z*): 337.1 $[M+H]^+$; HRMS for $C_{15}H_{17}FN_4O_2S$ $[M+H]^+$: 337.1135, Found: 337.1137.

4-Morpholino-1,2,5-thiadiazol-3-yl (4-fluorophenyl)(methyl)carbamate (JZP-MA-13, **6b**)

White solid (0.29 g, 40%); ^{1}H-NMR (400 MHz, DMSO-d_6): δ 7.51 (dd, J = 8.6, 4.8 Hz, 2H), 7.30 (t, J = 8.5 Hz, 2H), 3.66-3.61 (br s, 4H), 3.33-3-28 (br s, 7H); ^{13}C-NMR (101 MHz, DMSO-d_6): δ 162.26, 152.95, 150.10, 145.81, 137.96, 128.99 (2C), 116.37, 116.14, 65.52 (2C), 47.56 (2C), 38.62; ESI-MS (*m/z*): 339.1 $[M+H]^+$; HRMS for $C_{14}H_{15}FN_4O_3S$ $[M+H]^+$: 339.0927, Found: 339.0926.

4-(Piperidin-1-yl)-1,2,5-thiadiazol-3-yl methyl[4-(4,4,5,5-tetramethyl-1,3,2-dioxaborolan-2-yl)phenyl]carbamate (JZP-MA-17, **6c**)

White solid (0.2 g, 41%); ^{1}H-NMR (400 MHz, $CDCl_3$): δ 7.91-7.80 (m, 2H), 7.33 (d, J = 7.8 Hz, 2H), 3.43-3.39 (br s, 3H), 3.24-3.19 (br s, 4H), 1.53-1.47 (br s, 6H), 1.34 (s, 12H); ^{13}C-NMR (101 MHz, $CDCl_3$): δ 153.68, 151.06, 146.35, 144.66, 135.99 (4C), 125.86, 84.18 (2C), 49.11 (2C), 38.68, 25.51 (2C), 24.98 (4C), 24.25; ESI-MS (*m/z*): 445.2 $[M+H]^+$; HRMS for $C_{21}H_{29}BN_4O_4S$ $[M+H]^+$: 445.2085, Found: 445.2084.

4-Morpholino-1,2,5-thiadiazol-3-yl methyl[4-(4,4,5,5-tetramethyl-1,3,2-dioxaborolan-2-yl)phenyl]carbamate (JZP-MA-19, **6d**)

White solid (0.22 g, 46%); ^{1}H-NMR (400 MHz, $CDCl_3$): δ 7.87-7.82 (m, 2H), 7.31 (d, J = 7.8 Hz, 2H), 3.67-3.63 (s, 4H), 3.44-3.39 (s, 3H), 3.21-3.16 (br s, 4H), 1.34 (s, 12H); ^{13}C-NMR (101 MHz, $CDCl_3$): δ 152.89, 150.78, 146.26, 144.51, 136.06 (4C), 125.62, 84.26 (2C), 66.44 (2C), 48.14 (2C), 38.69, 24.99 (4C); ESI-MS (*m/z*): 447.1 $[M+H]^+$; HRMS for $C_{20}H_{27}BN_4O_5S$ $[M+H]^+$: 447.1877, Found: 447.1874.

4.2. Pharmacological evaluation and Assays:

***Determination of ABHD6, ABHD12 and MAGL activities using a sensitive fluorescent glycerol assay*:** Glycerol liberated from 1-AG hydrolysis was determined with a sensitive fluorescent glycerol assay using lysates of HEK293 cells expressing *h*ABHD6, *h*ABHD12 and *h*MAGL as previously described.[27] Briefly, glycerol production, which is coupled via an enzymatic cascade to generate resorufin, was kinetically monitored (0-90 min at RT, λ_{ex} 530;

λ_{em} 590 nm) using a Tecan Infinite M200 plate reader (Tecan Group Ltd, Männedorf, Switzerland). Cell lysates (99 µL, 0.3 µg protein/well) were preincubated for 30 min with the vehicle (DMSO) or the inhibitor (1 µL), after which the substrate (12.5 µM final concentration) was added (100 µL). The IC_{50}-values were calculated by Graphpad Prism version 5.00 for Windows, GraphPad Software, San Diego California USA, www.graphpad.com.

***Activity-based protein profiling (ABPP) of serine hydrolases*:** Competitive ABPP using mouse whole-brain, heart, liver or kidney homogenates was conducted to visualize the selectivity of inhibitors toward mouse ABHD6, ABHD12 and MAGL against other serine hydrolases in tissue proteomes. We used the active site serine-targeting fluorescent fluorophosphonate probe, carboxytetramethylrhodamine fluorophosphonate (TAMRA-FP; ActivX Fluorophosphonate Probes (FPs), Thermo Fisher Scientific Inc., Rockford, IL) as previously described.[27] Briefly, tissue homogenates (100 µg) were first treated for 1 h with DMSO or the selected inhibitors (with appropriate final concentrations ranging from 0.010-10 µM) at RT, after which TAMRA-FP labelling was conducted for 1 h at RT (final probe concentration 2 µM). The reaction was quenched by addition of a 2× gel loading buffer, after which samples with 10 µg protein were loaded per lane and the proteins were resolved in 10 % SDS-PAGE together with molecular weight standards. TAMRA-FP labeled serine hydrolases in samples were analysed by in-gel fluorescent gel scanning with the ChemiDoc™ MP imaging system (BIO-RAD, Hercules, California, USA) with Cy3 blot application (602/50, Green Epi, Manual Exposure 10 s–120 s).

Cyclic AMP (cAMP) assays: HEK293 cell lines stably expressing human CB_2 (hCB_2) with an amino-terminal haemagglutinin (HA) tag[56,57] and human CB_1 (hCB_1) with three amino-terminal HA tags[58,59] were cultured in high glucose Dulbecco's Modified Eagle's Medium (DMEM; Hyclone Laboratories, San Angelo, TX, USA) supplemented with 10% foetal bovine serum (FBS; New Zealand-origin, Moregate Biotech, Brisbane, Australia) and appropriate selection antibiotics, and incubated in 5% CO_2 at 37 °C in a humidified atmosphere.

Cellular cAMP levels were measured using a real-time BRET biosensor as described previously.[57,59] Briefly, cells were seeded in 10-cm dishes approximately 24 hours prior to transfection. The medium was then replaced with fresh medium and cells transfected with 5 µg of pcDNA3L-His-CAMYEL (ATCC, Manassas, VA, USA) using linear PEI (MW 25 kDa; Polysciences, Warrington, PA, USA) at a DNA:PEI ratio of 1:6. On the following day, cells were trypsinised and re-plated in white 96-well plates (Corning, Corning, NY, USA) treated with poly-D-lysine (Sigma-Aldrich, St. Louis, MO, USA) at a density of 50,000 cells per well.

Approximately 24 hours after plating (i.e. ~48 hours after transfection), cells were briefly washed with Hank's Balanced Salt Solution (HBSS; Thermo Fisher Scientific, catalogue #14025-134), then equilibrated for 30 minutes in HBSS supplemented with 1 $mg \cdot mL^{-1}$ low endotoxin bovine serum albumin (BSA; ICPBio, Auckland, NZ). Coelenterazine h (final concentration 5 µM; NanoLight Technologies, Pinetop, AZ, USA) was added to each well and incubated for 5 minutes in darkness, prior to dispensing vehicle/drugs (i.e. ABHD6 inhibitors in the presence of 5 µM forskolin ± cannabinoid ligands). All drugs and reagents were prepared in HBSS supplemented with 1 $mg \cdot mL^{-1}$ low endotoxin BSA, and all incubations and stimulations were performed at 37 °C. Cannabinoid ligand sources were: CP 55,940 from Cayman Chemical Company (Ann Arbor, MI, USA), SR141716A a kind gift from Roche Pharmaceuticals (Basel, Switzerland), and SR144528 from Abcam (Cambridge, UK).

Assays were carried out in technical duplicate and the positions of conditions were randomised between independent experiments to avoid the potential influence of any plate position effects. Emissions were detected at 460 nm (Rluc) and 535 nm (YFP) with a LUMIstar® Omega luminometer (BMG Labtech, Ortenberg, Germany). BRET ratios (535 nm / 460 nm, where an increase in ratio corresponds to a decrease in cAMP) were normalised to pre-drug reads (i.e., with coelenterazine h present only) to remove any variability present prior to addition of vehicle/drugs. Data were processed and analysed in GraphPad Prism using area under the curve analyses (v8; GraphPad Software Inc., La Jolla, CA, USA). Data were normalised to matched vehicle (0%) and forskolin (100%) treatments, allowing compilation of data from independent experiments.

4.3. Radiochemistry

The radiosynthesis was conducted on an automated synthesis module (Synthra RNplus, Synthra GmbH, Hamburg, Germany) with integrated preparative HPLC system (*Scheme S2*). ^{18}F-fluoride was produced on site *via* the nuclear reaction $^{18}O(p,n)^{18}F$ by irradiation of 2.0 mL $[^{18}O]H_2O$ (>98 atom % ^{18}O) using a "Cyclone Twin" 18 MeV cyclotron (IBA, Louvain-la-Neuve, Belgium) by running a beam current of 40 µA. Around 20-30 GBq was produced within 15 min (n=9). Quantification of starting activity was measured using CRC-25PET (Capintec Inc., USA) or VDC-505 (Veenstra, Netherlands) dose calibrators located in the hot cell. The eluate was directed after passage of UV-detector through a scintillation detector (Bioscan, Eckert & Ziegler, Germany) connected to a (single or multi) channel analyser for the analysis of radioactive compounds.

The analytical radio-HPLC (Method A): The chemical and radiochemical purity of the compounds were determined using Agilent Eclipse Plus, with a HPLC pump equipped with a

UV detector using a C18 column (C18, 5 µM, 4.6 mm × 150 mm). The analytical HPLC column was eluted with a 0.1 M NH_4Oac in H_2O or H_2O (A) and MeCN (B) using a gradient at a flow rate of 1.0 mL/min (0-10 min 5% to 95% B, 10-15 min 95% B, 15-17 min 95% to 5% B). (Method B): The preparative HPLC was carried out using Agilent Zorbax Eclipse XDB-C18 (9.4 mm × 250 mm, 5 µm) using MeCN/H_2O (60/40, v/v) or NH_4OAc (0.1 M) (60/40, v/v) with a flow rate 4.0 mL/min.

Automated Radiosynthesis on Synthra RN plus (UQ, Brisbane): At the end of bombardment (EOB), the aqueous solution of [^{18}F]-fluoride was transferred to the synthesis module where the [^{18}F]-fluoride was extracted from the solution using an anion exchange cartridge (Sep-Pak Light 46 mg, Waters, Part No. 186004540). ^{18}F-Fluoride was then trapped on an QMA cartridge [^{18}F]fluoride was then eluted with a freshly prepared tetraethylammonium bicarbonate solution (2 mg/mL) in anhydrous MeOH (2 mL). After drying (~5 min at 68 °C then at 130 °C for ~6 min), a mixture of the precursor JZP-MA-17 (10.0 µmol, 4.46 mg) and catalyst $[Cu(Py)_4](OTf)_2$ (10.0 µmol, 6.78 mg) in anhydrous DMA (500 µL) from A3 was added to the reactor containing dried [^{18}F]Et_4NF. The reaction was carried out at 110 °C for 20 min, after cooling down to 30 °C, the reaction was quenched with 500 µL of MeCN/NH_4OAc (0.1 M) (60/40, v/v). The purification was carried out using preparative HPLC (Agilent Zorbax Eclipse XDB-C18 (9.4 mm × 250 mm, 5 µm) using MeCN/H_2O or NH_4OAc (0.1 M) (60/40, v/v) at a flow rate 4 mL/min. The radioactive peak corresponding to [^{18}F]JZP-MA-11 (t_R ~19 min in *Scheme S2*) was collected, diluted with H_2O (40 mL) and loaded on C18 SPE cartridge and the cartridge was subsequently washed with 10 mL water. [^{18}F]JZP-MA-11 was eluted from the cartridge using 0.8 mL ethanol (EtOH), sterile filtered (Millex-GV filter 0.22 µm 13 mm, Sigma-Aldrich, SLGV013SL) and formulated for animal studies using NaCl 0.9% (6 mL). The identity and radiochemical purity of [^{18}F]JZP-MA-11 was determined using an analytical HPLC (Agilent Eclipse Plus column, C18, 4.6 mm × 150 mm) eluted using MeCN/NH_4OAc (0.1 M) at 1 mL/min on a gradient run. [^{18}F]JZP-MA-11 (10 µL) was spiked with its non-radioactive analogue (10 µL, 1 mg/mL) to confirm its identity (*Figure 3*). The radiochemical purity of [^{18}F]JZP-MA-11was found to be >99% and and a molar activity of 180±110 GBq/µmol (n=9). Total radioactivity (0.38–1.69 GBq, n=9) was assayed in a volume of 5.8 mL. The radiochemical purity was about 97% at 210 min postproduction, indicating that the tracer is stable in the batch vehicle at the obtained tracer concentration. The overall synthesis time including HPLC-SPE purification and reformulation was 71 min from EOB. The non decay corrected radiochemical yield was 3.2% (n.d.c, n=9). Retention time (t_R) in the analytical RP-

HPLC system was, t_R [^{18}F]JZP-MA-11 = ~11.0 min (HPLC method A). Retention time on the semi-preparative RP-HPLC system t_R [^{18}F]JZP-MA-11 = ~19.0 min (HPLC method B).

Automated Radiosynthesis on Trasis AIO (KU Leuven, Belgium):

[^{18}F]fluoride was produced by a 30 min irradiation of 2 mL of 97 % enriched [^{18}O]H_2O in a niobium target with 18-MeV protons from a Cyclone 18/9 cyclotron (Ion Beam Applications, Louvain-la-Neuve, Belgium) and transferred to the Trasis All-In-One (AIO) synthesizer (Trasis, Ans, Belgium) located in a lead shielded hot cell (Comecer, Castel Bolognese, Italy). Separation from the [^{18}O]H_2O was performed using a QMA carbonate plus light 46 mg cartridge (Waters). The [^{18}F]fluoride was eluted from the QMA into the reactor with a solution of TEAB (4.2 mg, 0.6 mL) in a mixture of DI water and CH_3CN (30/70 V/V), dried under a N_2 flow and reduced pressure at 125 °C and further dried azeotropically with anhydrous CH_3CN (0.75 mL) under a N_2 flow and reduced pressure at 125 °C. A solution of the boronate ester precursor JZP-MA-17 (5.0 µmol, 2.2 mg) and the catalyst $[Cu(Py)_4](OTf)_2$ (9.0 µmol, 6.1 mg) in anhydrous DMA (700 µL) was added to the dried [^{18}F]fluoride-TEAB, and the reaction mixture was heated at 110 °C for 20 min. After cooling down, the reaction mixture was diluted with a mixture of NH_4COOH 50 mM and CH_3CN (3 mL; 77/23 V/V) and injected onto a semi-preparative XTerra C18 HPLC column (5 µm, 7.8 x 150 mm; Waters) eluted with mixtures of NH_4COOH 50 mM and CH_3CN (55/45 V/V) at a flow rate of 3 mL/min. UV detection was performed at 309 nm. The HPLC fraction containing the radioactive product peak [^{18}F]JZP-MA-11 (retention time ~ 22 min) was diluted with NaCl 0.9% (10 mL) and reformulated using a C18 SepPak light cartridge (Waters; preconditioned with 5 ml ethanol and 10 ml water). After loading, the SepPak was washed with 5 ml NaCl 0.9 %. The tracer was eluted from the SepPak with 0.7 mL ethanol and the SepPak was additionally rinsed with 6.3 mL NaCl 0.9% to obtain the final [^{18}F]JZP-MA-11 in 7 mL vehicle composed of 10 % (V/V) ethanol in NaCl 0.9%.
Quality control was performed using an analytical HPLC system consisting of an XBridge C18 column (3.5 µm; 3 x 100 mm; Waters) eluted with mixtures of NH_4COOH 50 mM and CH_3CN (55/45 V/V) at a flow rate of 0.7 mL/min. UV detection was performed at 309 nm. [^{18}F]JZP-MA-11 was prepared in a total synthesis time of 1 h 20 min, with a radiochemical yield of 1.4 ± 0.3 % (decay corrected), a radiochemical purity ≥ 99 % and an average molar activity of 418 ± 73 GBq/µmol (n= 4).

4.4. Preclinical Evaluation

***4.4.1. In vivo* PET/CT imaging:** All animal experiments were approved by the University of Queensland Ethics committee and carried out at the Centre for Advanced Imaging, UQ. PET/CT images were acquired using an Inveon multimodality PET/CT scanner (Siemens). On the experimental days, 6 healthy female C57BL/6 mice (10-12-week-old) were anaesthetized with 2–3% isoflurane (Isothesia, Piramal Enterprises Limited, India) in oxygen at a flow of 1 L/min. A catheter was inserted into the lateral tail vein before the animal was placed in the scanner. Mice were maintained under 1–2% isoflurane in air-oxygen mixture at a flow rate of 1 L/min for the duration of the imaging session. Physiological monitoring (respiratory using a sensor probe) was achieved throughout all experiments using an animal monitoring system (BioVet system, m2 m Imaging, Australia). The mice (n=6) were injected with 150 µL of [^{18}F]JZP-MA-11 (1.05 ± 0.492 MBq, mean ± SD) in the above specified tracer batch vehicle. A 60-min dynamic PET scan was started simultaneously with the tracer injection and was followed by a 10-min CT attenuation scan.

For the *in vivo* blocking study, mice were first injected with unlabelled JZP-MA-11 (*i.v.*, 1.5 mg/kg in 10%DMSO/5%Tween/Saline) or WWL70 (*i.p.*, 0.75 mg/kg in 40%DMSO/5%Tween/Saline). Twenty minutes later, [^{18}F]JZP-MA-11 (1.88 ± 0.080 MBq, mean ± SD; 150 µL in tracer batch vehicle) was administered through tail vein injection. A 60 min dynamic PET scan was started simultaneously with the tracer injection and was followed by a 10 min CT attenuation scan.

The CT images of the mice were acquired through an X-ray source with the voltage set to 80 kV and the current set to 500 µA. The scans were performed using 360° rotation with 120 rotation steps with a low magnification and a binning factor of four. The exposure time was 230 ms with an effective pixel size of 106 µm. The CT images were reconstructed using a Feldkamp conebeam back-projection algorithm provided by an Inveon Acquisition Workstation (IAW 2.1, Siemens). For the dynamic PET data acquisition, the emission data were normalized and corrected for radioactive decay. The list-mode data were sorted into 29 time frames (10 × 30s, 10 × 60s, 9 × 300s). The resulting sinograms were reconstructed with an ordered-subset expectation maximization (OSEM2D) algorithm and analysed using the Inveon Research Workplace software (IRW 4.1, Siemens) which allows fusion of CT and PET images and definition of region of interest (ROIs). For each PET image, 3D ROIs were drawn over the brain and other organs of interest guided by the CT using the IRW 4.1 software. Activity per voxel was converted to nCi/cc using a conversion factor obtained by scanning a

cylindrical phantom filled with a known activity of [^{18}F]fluoride to account for PET scanner efficiency. Activity concentrations were then expressed as percent of the decay-corrected injected activity per cm^3 of tissue that can be approximated as percentage injected dose/g (%ID/g). The mean value in each ROI was used to generate regional time activity curves (TACs). Individual TACs were normalized by the injected dose and the animal weight, and then expressed in standardized uptake value (SUV-BW). TACs were drawn for each organ of interest including brain, heart, liver, kidney, guts and bladder.

Extent of irreversible binding in Brain: Healthy female C57BL6 mice (10-12-weel-old) (n = 3) were anesthetized with isoflurane (2.5% in O_2 at 1 L/min) and injected intravenously (*i.v.*) with [^{18}F]JZP-MA-11 (10.63 ± 3.18 MBq) of the tracer *via* tail vein. At 30 min post injection, a cardiac perfusion with saline was performed on deep anaesthetized mice, the mouse brain was removed and homogenized in an ice-cold acetonitrile (MeCN) (1 mL) solution. The homogenate was centrifuged for 10 min at 4000 rpm and supernatant was collected. The supernatants and the pellets were counted for radioactivity.

4.4.2 Autoradiography

***In vitro* autoradiography:** Coronal cryo-sections (20 µm) of healthy female C57BL/6 mouse brain were obtained using a cryotome (Shandon cryotome FSE, Thermo Fisher Scientific, Waltham, USA), and mounted on adhesive microscope slides (Superfrost Plus; Thermo Fisher Scientific) and stored at -20 °C. The tissue slices were pre-incubated with an incubation buffer (50 mM Tris-HCl, pH 7.4, containing 1% bovine serum albumin (BSA)) for 10 min at room temperature. To assess specificity of binding, some slides (n=5-7) were incubated with 100 nM of [^{18}F]JZP-MA-11 alone (~73 kBq/20 µL). Adjacent slides (n=5-7) were incubated with a mixture of 100 nM of [^{18}F]JZP-MA-11 in the presence of WWL70 (10, 50 and 100 µM) dissolved in DMSO (10%) or the tracer in presence of reference material (JZP-MA-11; 20 µM) dissolved in 10% EtOH (n=5-7). After incubation for 30 minutes at room temperature, slides were washed three times with a washing buffer (50 mM Tris-HCl, pH 7.4 containing 1% BSA/EtOH (70/30) for 1 min each. The tissue sections were then quickly washed in distilled water for three successive washes to remove excess of buffer salts. Dried slices were exposed to a phosphor imager plate (BAS-IP MS 2040, FujiFilm, Japan) overnight and the plate was scanned in an AmershamTyphoon Biomolecular Imager (GE Healthcare, USA). The data was analyzed using ImageQuant TL image analysis software (GE Healthcare). The radioactivity distribution in the slides was expressed as digital light units/mm^2 (DLU/mm^2) corrected for background. Percentage block *vs* control was calculated as (DLU/mm^2 in the

presence of 10, 50 or 100 μM WWL70 (blocker)) / (DLU/mm^2 tracer only) on 5-7 tissue sections from the same experiment.

***Ex Vivo* Autoradiography:** Healthy female C57BL/6 mice (10-12-week-old) (n = 3) were injected with [^{18}F]JZP-MA-11 (12.8 ± 1.82 MBq, mean ± SD) *via* a tail vein catheter under anesthesia (2.5 % isoflurane in O2 at 1 L/min flow rate) and were perfused with saline under anesthesia at 30 min post-tracer injection. Brains were removed and rapidly frozen in 2-methylbutane (Fisher Scientific, UK) on dry ice (between −42 and −44 °C). Coronal sections (20 μm) mounted on adhesive microscope slides (Superfrost Plus, Thermo Scientific, Germany) were obtained using a cryotome (CM3050S, Leica, Germany), dried and exposed to a phosphor storage screen film (BAS-IP MS 2040, FujiFilm, Japan) overnight. The screens were read using an Amersham Typhoon Biomolecular Imager (GE Healthcare, USA) and analyzed using ImageQuant TL image analysis software from GE Healthcare. To further demonstrate the binding specificity of [^{18}F]JZP-MA-11, we performed an *ex vivo* blocking study. Mice (n=2) were first injected *i.v.* with the authentic reference compound ^{19}F-JZP-MA-11 (1.50 mg/kg in 10%DMSO/5%Tween/Saline), 20 minutes later, [^{18}F]JZP-MA-11 (7.34 ± 1.00 MBq, mean ± SD) was administered also through tail vein injection. At 30 min after tracer injection, the mice were sacrificed and the brain were removed and sectioned and exposed to the phosphor storage screen as described in the section above. For the quantification, regions-of-interest (ROIs) were drawn on the brain images from each mouse (n=10 brain sections were used to draw ROIS from each brain region) using an irregular shaped drawing tool, to measure the amount of radioactivity in each of the brain regions. Similar ROIs were drawn in a background region (n=10 regions) to enable background subtraction. The results were expressed as digital light units per square millimeter normalized for body weight of the animal and injected dose [(DLU/mm^2) × (body weight/injected dose)].

4.4.3. Metabolite Analysis

The [^{18}F]JZP-MA-11 (~10 ± 2 MBq, mean ± SD) was administered in healthy female C57BL/6 mouse *via* tail vein catheter. Thirty minutes after administration of the radioligand, the animals (n = 2) were sacrificed, and the organs of interest (brain, kidneys, liver and heart) were harvested and blood collected in heparin-coated tube. The organs were homogenized using a homogenizer (Labserv D130, Thermo Fischer Scientific, Australia), the radioactivity in organs was extracted by adding 1 mL of MeCN (100%) then homogenized samples were centrifuged at 5000 *g* for 5 min. Plasma was separated from the blood cells by centrifugation at 5000 *g* for

5 min. The radioactivity from 200 µL of plasma sample was extracted with 200 µL of MeCN (100%) followed by centrifugation at 5000 *g* for 5 min. Aliquots of the extracted organ homogenates and plasma (5 µL) were spotted onto TLC plates. For normal phase (25% EtOAc/Hexane) and reverse phase (33% 0.1 M NH_4OAc/MeCN) were used as mobile phase solvents. The TLC plates were exposed to a phosphor storage screen film (BAS-IP MS 2040, FujiFilm, Japan) overnight. The screens were read using an Amersham Typhoon Biomolecular Imager (GE Healthcare, USA) and analyzed using ImageQuant TL image analysis software from GE Healthcare. Representative TLC images are shown in *Scheme S7*.

4.4.4. In vivo PET/MRI imaging

Anaesthetized healthy Sprague-Dawley rats (male, 10-12-week-old, n=3), with a cannulated tail vein, (0.020”× 0.060”OD Tygon microbore tubing, 30 cm long, and 26 gauge needles) were placed in a combined MRI/PET system, comprising a 300mm bore 7T ClinScan, running Siemens VB17, and removable PET insert containing 3 rings of 16 detector blocks with 15X15 LSO crystals (1.6 mm × 1.6 mm × 10 mm) per block, at the centre of the magnet bore operating under Siemens Inveon Acquisition Workplace (IAW) (Bruker, Germany). A 40 mm ID rat head MRI rf coil inside the PET ring was used to acquire rat head images simultaneously with the PET acquisition. Rats were maintained under 1% to 2% isoflurane in an air-oxygen mixture at a flow rate of 1 L/min for the duration of the imaging session and monitored by a breathing pillow.

Following localiser images, the PET acquisition (60 min) was started. After 2 min of baseline scanning, the rats were injected with a solution of [^{18}F]JZP-MA-11 (29.3 ± 6.31 MBq) in saline/EtOH in a total volume of 500 µL. During the PET scanning, anatomical images were acquired including T2 weighted anatomical images (*Scheme S8B*) with the following parameters: Field-of-view = 40 mm × 40 mm, slice thickness = 0.6 mm, number of slices = 50, in-plane resolution = 0.156 mm × 0.156 mm, TR = 7200, TE = 36, turbo factor =11, averages = 6, image time = 17:31 min.

The list-mode data were sorted into 20 dynamic frames (10 × 60 s, 10 × 300 s, time frames). The resulting sinograms were reconstructed with a two dimensional ordered-subset expectation maximization (OSEM2D) algorithm. The dynamic PET images were registered and displayed with the T2-weighted MRI images using Siemens Inveon Research Workplace (IRW version 4.1, Siemens). The T2-weighted MRI images, display excellent anatomical resolution and contrast and were used to delineate region of interest throughout the brain.

4.4.5. MALDI-2 imaging

Tissue samples preparation for MALDI-2: Tissue samples of the healthy female C57BL/6 mouse brain were generated in-house as follows. Mice were injected with unlabelled JZP-MA-11 (i.v., 1.0 mg/kg in 10%DMSO/5%Tween/Saline) or vehicle. After 30 mins, brain were removed and rapidly frozen in methylbutane (Fisher Scientific, UK) on dry ice (between −42 and −44 °C). The coronal tissue sections (20 µm) were obtained using a cryotome (CM3050S, Leica, Germany) and subsequently mounted onto indium-tin oxide (ITO) coated glass slides and stored frozen at −20 °C prior to use.

Matrix Vapour deposition: Matrix deposition was carried out using an in-house built sublimation apparatus. 40 µL 2,5-dihydroxybenzoic acid saturated acetone was placed into the bottom of the sublimation device and allowed to evaporate. The brain tissue mounted ITO glass slides were mounted onto the water-cooled element of the device. After closing the apparatus, the vacuum was generated using a vaccum pump and the hot plate was heated to a surface temperature of 140 °C. The vacuum was applied until 0.9 mbarr was reached. Once the chamber had returned to atmospheric pressure, the slide was remove and sprayed with a solution of 50% methanol (aq) with 0.2% trifluoroacetic acid using an imageprep (Bruker) piezo sprayer to facilitate recrystalisation of the DHB with the analytes in the tissue - a customised program of 20 cycles including 2 seconds spray time, 30 seconds incubation, 20 seconds dry.

Instrument parameters tims-TOF Flex with MALDI-2: The prepared tissue sample was analysed using a timsTOF Flex equipped with MALDI-2 using the following methodology operating in QqTOF mode. The instrument was externally calibrated using $[M+H]^+$ and $[2M+H]^+$ for alpha-cyano-4-hydroxycinnamic acid and ESI calibration solution (Fluka, 63606). MALDI-MSI was performed in positive mode over a mass range of m/z 100-1,000 at 50 µm spatial resolution with beam scan on. Spectra were accumulated from 300 laser shots at 1 kHz frequency. Data was visualised using SCILS LAB MVS 2021.

4.5. PET Imaging in NHP.

The imaging experiment in the macaque was conducted according to the Belgian code of practice for the care and use of animals, after approval from the local University Ethics Committee for Animals at the Katholieke Universiteit Leuven, Belgium. Baseline uptake was

established in one male rhesus monkey (*Macaca mulatta*, n=1, 10.4 kg). The macaque was sedated (~75 min before tracer injection) by an intramuscular (i.m.) injection of a combination of 0.3 mL Rompun (xylazine 2% solution) and 0.35 mL Nimatek (ketamine 100 mg/mL). About 60 min after the first injection, the monkey received an additional dose of 0.15 mL Rompun and 0.175 mL Nimatek *via i.v.* injection. O_2 and CO_2 saturation in the blood and heart rate were constantly monitored during scanning, and body temperature was maintained via an electronically controlled heating pad. A venous line was inserted for administration of the radiotracer and for collection of venous blood for radiometabolite analysis.

PET and MR image acquisition: Scans were acquired using the Focus™ 220 microPET scanner (Concorde Microsystems, Knoxville, TN, USA). Before radiotracer injection, a 10-min transmission scan using a ^{57}Co source was obtained to assess positioning and for subsequent attenuation correction. A 120-min dynamic PET scan was acquired in list mode concurrently with the injection of [^{18}F]JZP-MA-11 (210 MBq, manual bolus over 30 sec, vena saphena). Data were histogrammed into 4 × 15s, 4 × 60s, 5 × 180s, 8 × 300s and 6 × 600s timeframes and reconstructed using the MAP algorithm (18 iterations, resolution 1.5 mm) with attenuation correction into 256 × 256 × 95 pixels. No scatter correction was applied.

A three-dimensional T1-weighted MR scan of the monkey was obtained for co-registration purposes on a 3.0 Tesla full-body scanner (Tim Trio Scanner, Siemens) using a magnetization prepared rapid gradient echo (MPRAGE) sequence (*tfl3d1_16) with the following parameters: repetition time 2700 ms, echo time 3.8ms, inversion time 850ms, Flip angle 9°, 256 × 208 ×144 matrix, 0.6mm voxel size.

Venous blood sampling and plasma radiometabolite analysis: Venous blood sampling was performed manually (*via* a 3-way valve) at preselected time points (10, 30 and 60 min post tracer injection). All collected blood samples (in 4-mL BD Vacutainer K2EDTA tubes) were immediately stored on ice to stop metabolism. After centrifugation (2330 × g, 5 min), the plasma was processed and analysed using HPLC to quantify the fraction of intact tracer at the different time points. To about 0.5 mL of plasma, an equal amount of MeCN was added and the resulting suspension was centrifuged (2330 × g, 5 min) to separate the precipitated proteins from the supernatant. Next, about 0.8 mL of supernatant was filtered through a syringe filter (0.22 µm; Millipore), diluted with water (1/2 of the volume) and spiked with authentic JZP-MA-11. A volume of about 1 mL of extract was injected onto an HPLC system consisting of an analytical XTerra column (C18; 5 µm, 4.6 mm × 250 mm, Waters) eluted with a mixture of

0.05 M NH_4COOH and MeCN (45/55 v/v) at a flow rate of 1 mL/min. After passing through a UV detector (309 nm) and a shielded 3-in. NaI(Tl) scintillation detector connected to a multichannel analyzer (Gabi box, Raytest, Straubenhardt Germany), the HPLC eluate was collected as 1-mL fractions using an automated fraction collector. Radioactivity in the filtered plasma (prior to HPLC), filter, and HPLC eluent fractions was counted in a well-type gamma counter equipped with a 3-in NaI(Tl) well crystal coupled to a multichannel analyzer (Wallac 1480 Wizard, Wallac, Turku, Finland). The results were corrected for background radiation, detector dead-time and physical decay during counting.

Imaging analysis: PET data were averaged and coregistered to the MRI image which was in turn normalized to a macaque atlas.[60] Dynamic PET data were then transformed to the atlas space to generate time activity curves. All operations were carried out using the PFUS module of PMOD 4.0 (PMOD, Switzerland).

5. Acknowledgments

M.A., I.B., K.T. thank the Australian Research Council Training Centre for Innovation in Biomedical Imaging Technology (project number IC170100035) for funding. M.A. acknowledges the UQ Early Career Research Fellowship, 2020 (UQECR2057937). J.Z.P would like to thank the Academy of Finland (grant no. 322724) for funding. K.T. acknowledges the National Health and Medical Research Council for a Career Development Fellowship (APP1148582). Parts of this research was conducted and funded by the ARC Centre of Excellence in Convergent Bio-Nano Science and Technology (CE140100036). C.C, was funded by the Fonds Wetenschappelijk Ondezoek (FWO I000321N). The authors acknowledge the facilities, scientific and technical assistance of the National Imaging Facility, a National Collaborative Research Infrastructure Strategy (NCRIS) capability, at the Centre for Advanced Imaging and the Centre for Microscopy and Microanalysis, The University of Queensland.

Competing Interests

All the authors declare that they do not have any competing interests.

Ethics Statement

All animal care and experimental procedures were carried with the approval of the Animal Ethics Committee of The University of Queensland (CAI/082/20) and following the guiding principles of the Australian Code for the Care and Use of Animals for Scientific Purposes. The imaging experiment in the macaque was conducted according to the Belgian code of practice

for the care and use of animals, after approval from the local University Ethics Committee for Animals at the Katholieke Universiteit Leuven, Belgium.

Abbreviations

XYZ

Author Contributions

M.A. conceived the study and designed the experiments. M.A., K.M., J.Z.P., J.R.S., D.S., C.O., M.A.M., G.C., B.R.H., G.F.M.N. performed research. M.A., K.M., N.G., J.R.S., G.C. analyzed the data. J. Y. -K., I.B., R.B., K.J.T. supervised the project. W.V. provided the NHP for the study. S.C., C.C. carried out the NHP study and S.C., C.C., M.A. analyzed the NHP data. G.B. supervised the NHP study. M.A. wrote the manuscript and all other authors contributed, reviewed and edited the manuscript.

6. References:

(1) Varlow, C.; Boileau, I.; Wey, H.-Y.; Liang, S. H.; Vasdev, N. Classics in Neuroimaging: Imaging the Endocannabinoid Pathway with PET. *ACS Chem Neurosci* **2020**, *11*, 1855–1862. https://doi.org/10.1021/acschemneuro.0c00305.

(2) Van Laere, K. In Vivo Imaging of the Endocannabinoid System: A Novel Window to a Central Modulatory Mechanism in Humans. *European Journal of Nuclear Medicine and Molecular Imaging*. **2007**, 1719–1726. https://doi.org/10.1007/s00259-007-0505-3.

(3) Stasiulewicz, A.; Znajdek, K.; Grudzień, M.; Pawiński, T.; Sulkowska, J. I. A Guide to Targeting the Endocannabinoid System in Drug Design. *Int J Mol Sci* **2020**, *21* (8). https://doi.org/10.3390/ijms21082778.

(4) Grimsey, N. L.; Savinainen, J. R.; Attili, B.; Ahamed, M. Regulating Membrane Lipid Levels at the Synapse by Small-Molecule Inhibitors of Monoacylglycerol Lipase: New Developments in Therapeutic and PET Imaging Applications. *Drug Discovery Today*. **2020**, 330–343. https://doi.org/10.1016/j.drudis.2019.10.004.

(5) Bowman, A. P.; Heeren, R. M. A.; Ellis, S. R. Advances in Mass Spectrometry Imaging Enabling Observation of Localised Lipid Biochemistry within Tissues. *TrAC - Trends in Analytical Chemistry*., **2019**, 115197. https://doi.org/10.1016/j.trac.2018.07.012.

(6) Porta Siegel, T.; Hamm, G.; Bunch, J.; Cappell, J.; Fletcher, J. S.; Schwamborn, K. Mass Spectrometry Imaging and Integration with Other Imaging Modalities for Greater Molecular Understanding of Biological Tissues. *Molecular Imaging and Biology*. **2018**, 888–901. https://doi.org/10.1007/s11307-018-1267-y.

(7) Wymann, M. P.; Schneiter, R. Lipid Signalling in Disease. *Nature Reviews Molecular Cell Biology*., **2008**, 162–176. https://doi.org/10.1038/nrm2335.

(8) Baggelaar, M. P.; Maccarrone, M.; van der Stelt, M. 2-Arachidonoylglycerol: A Signaling Lipid with Manifold Actions in the Brain. *Prog Lipid Res* **2018**, *71*, 1–17. https://doi.org/10.1016/J.PLIPRES.2018.05.002.

(9) Katona, I.; Freund, T. F. Endocannabinoid Signaling as a Synaptic Circuit Breaker in Neurological Disease. *Nature Medicine*., **2008**, 923–930. https://doi.org/10.1038/nm.f.1869.

(10) Cabral, G. A.; Griffin-Thomas, L. T. Emerging Role of the Cannabinoid Receptor CB 2 in Immune Regulation: Therapeutic Prospects for Neuroinflammation. *Expert Reviews in Molecular Medicine*. Cambridge University Press December 2009. https://doi.org/10.1017/S1462399409000957.

(11) Di Marzo, V. Endocannabinoid Signaling in the Brain: Biosynthetic Mechanisms in the Limelight. *Nat Neurosci* **2011**, *14* (1), 9–15. https://doi.org/10.1038/nn.2720.

(12) Kind, L.; Kursula, P. Structural Properties and Role of the Endocannabinoid Lipases ABHD6 and ABHD12 in Lipid Signalling and Disease. *Amino Acids*., **2019**, 151–174. https://doi.org/10.1007/s00726-018-2682-8.

(13) Li, F.; Fei, X.; Xu, J.; Ji, C. An Unannotated α/β Hydrolase Superfamily Member, ABHD6 Differentially Expressed among Cancer Cell Lines. *Mol Biol Rep* **2009**, *36* (4), 691–696. https://doi.org/10.1007/s11033-008-9230-7.

(14) Baggelaar, M. P.; van Esbroeck, A. C. M.; van Rooden, E. J.; Florea, B. I.; Overkleeft, H. S.; Marsicano, G.; Chaouloff, F.; van der Stelt, M. Chemical Proteomics Maps Brain Region Specific Activity of Endocannabinoid Hydrolases. *ACS Chem Biol* **2017**, *12* (3), 852–861. https://doi.org/10.1021/acschembio.6b01052.

(15) Schlosburg, J. E.; Blankman, J. L.; Long, J. Z.; Nomura, D. K.; Pan, B.; Kinsey, S. G.; Nguyen, P. T.; Ramesh, D.; Booker, L.; Burston, J. J.; Thomas, E. A.; Selley, D. E.; Sim-Selley, L. J.; Liu, Q. S.; Lichtman, A. H.; Cravatt, B. F. Chronic Monoacylglycerol Lipase Blockade Causes Functional Antagonism of the Endocannabinoid System. *Nat Neurosci* **2010**, *13* (9), 1113–1119. https://doi.org/10.1038/nn.2616.

(16) Schlosburg, J. E.; Kinsey, S. G.; Ignatowska-Jankowska, B.; Ramesh, D.; Abdullah, R. A.; Tao, Q.; Booker, L.; Long, J. Z.; Selley, D. E.; Cravatt, B. F.; Lichtman, A. H. Prolonged Monoacylglycerol Lipase Blockade Causes Equivalent Cannabinoid Receptor Type 1 Receptor-Mediated Adaptations in Fatty Acid Amide Hydrolase Wild-Type and Knockout Mice. *Journal of Pharmacology and Experimental Therapeutics* **2014**, *350* (2), 196–204. https://doi.org/10.1124/jpet.114.212753.

(17) Cao, J. K.; Kaplan, J.; Stella, N. ABHD6: Its Place in Endocannabinoid Signaling and Beyond. *Trends in Pharmacological Sciences*., **2019**, 267–277. https://doi.org/10.1016/j.tips.2019.02.002.

(18) Chicca, A.; Arena, C.; Manera, C. Beyond the Direct Activation of Cannabinoid Receptors: New Strategies to Modulate the Endocannabinoid System in CNS-Related Diseases. *Recent patents on CNS drug discovery*. **2016**, pp 122–141. https://doi.org/10.2174/1574889810999160603185126.

(19) Poursharifi, P.; Madiraju, S. R. M.; Prentki, M. Monoacylglycerol Signalling and ABHD6 in Health and Disease. *Diabetes, Obesity and Metabolism*., **2017**, 76–89. https://doi.org/10.1111/dom.13008.

(20) Naydenov, A. v.; Horne, E. A.; Cheah, C. S.; Swinney, K.; Hsu, K. L.; Cao, J. K.; Marrs, W. R.; Blankman, J. L.; Tu, S.; Cherry, A. E.; Fung, S.; Wen, A.; Li, W.; Saporito, M. S.; Selley, D. E.; Cravatt, B. F.; Oakley, J. C.; Stella, N. ABHD6 Blockade Exerts Antiepileptic Activity in PTZ-Induced Seizures and in Spontaneous Seizures in R6/2 Mice. *Neuron* **2014**, *83* (2), 361–371. https://doi.org/10.1016/j.neuron.2014.06.030.

(21) Zhao, S.; Mugabo, Y.; Ballentine, G.; Attane, C.; Iglesias, J.; Poursharifi, P.; Zhang, D.; Nguyen, T. A.; Erb, H.; Prentki, R.; Peyot, M. L.; Joly, E.; Tobin, S.; Fulton, S.; Brown, J. M.; Madiraju, S. R. M.; Prentki, M. α/β-Hydrolase Domain 6 Deletion Induces Adipose Browning and Prevents Obesity and Type 2 Diabetes. *Cell Rep* **2016**, *14* (12), 2872–2888. https://doi.org/10.1016/j.celrep.2016.02.076.

(22) Zhao, S.; Mugabo, Y.; Iglesias, J.; Xie, L.; Delghingaro-Augusto, V.; Lussier, R.; Peyot, M. L.; Joly, E.; Taïb, B.; Davis, M. A.; Brown, J. M.; Abousalham, A.; Gaisano, H.; Madiraju, S. R. M.; Prentki, M. α/β-Hydrolase Domain-6-Accessible Monoacylglycerol Controls Glucose-Stimulated Insulin Secretion. *Cell Metab* **2014**, *19* (6), 993–1007. https://doi.org/10.1016/j.cmet.2014.04.003.

(23) Cao, J. K.; Viray, K.; Shin, M.; Hsu, K.-L.; Mackie, K. ABHD6 Inhibition Rescues a Sex-Dependent Deficit in Motor Coordination in The HdhQ200/200 Mouse Model of Huntington's Disease. *J Neurol Neurol Disord* **2021**, *7* (1), 106.

(24) Tang, Z.; Xie, H.; Heier, C.; Huang, J.; Zheng, Q.; Eichmann, T. O.; Schoiswohl, G.; Ni, J.; Zechner, R.; Ni, S.; Hao, H. Enhanced Monoacylglycerol Lipolysis by ABHD6 Promotes NSCLC Pathogenesis. *EBioMedicine* **2020**, *53*, 102696. https://doi.org/10.1016/j.ebiom.2020.102696.

(25) Hou, L.; Rong, J.; Haider, A.; Ogasawara, D.; Varlow, C.; Schafroth, M. A.; Mu, L.; Gan, J.; Xu, H.; Fowler, C. J.; Zhang, M.-R.; Vasdev, N.; Ametamey, S.; Cravatt, B. F.; Wang, L.; Liang, S. H. Positron Emission Tomography Imaging of the Endocannabinoid System: Opportunities and Challenges in Radiotracer Development. *J. Med. Chem* **2021**, *64*, 123–149. https://doi.org/10.1021/acs.jmedchem.0c01459.

(26) Patel, J. Z.; Nevalainen, T. J.; Savinainen, J. R.; Adams, Y.; Laitinen, T.; Runyon, R. S.; Vaara, M.; Ahenkorah, S.; Kaczor, A. A.; Navia-Paldanius, D.; Gynther, M.; Aaltonen, N.; Joharapurkar, A. A.; Jain, M. R.; Haka, A. S.; Maxfield, F. R.; Laitinen, J. T.; Parkkari, T. Optimization of 1,2,5-Thiadiazole Carbamates as Potent and Selective

ABHD6 Inhibitors. *ChemMedChem* **2015**, *10* (2), 253–265. https://doi.org/10.1002/cmdc.201402453.

(27) Navia-Paldanius, D.; Savinainen, J. R.; Laitinen, J. T. Biochemical and Pharmacological Characterization of Human α/β-Hydrolase Domain Containing 6 (ABHD6) and 12 (ABHD12). *J Lipid Res* **2012**, *53* (11), 2413–2424. https://doi.org/10.1194/jlr.M030411.

(28) Hsu, K. L.; Tsuboi, K.; Chang, J. W.; Whitby, L. R.; Speers, A. E.; Pugh, H.; Cravatt, B. F. Discovery and Optimization of Piperidyl-1,2,3-Triazole Ureas as Potent, Selective, and in Vivo-Active Inhibitors of α/β-Hydrolase Domain Containing 6 (ABHD6). *J Med Chem* **2013**, *56* (21), 8270–8279. https://doi.org/10.1021/jm400899c.

(29) Patel, J. Z.; Parkkari, T.; Laitinen, T.; Kaczor, A. A.; Saario, S. M.; Savinainen, J. R.; Navia-Paldanius, D.; Cipriano, M.; Leppänen, J.; Koshevoy, I. O.; Poso, A.; Fowler, C. J.; Laitinen, J. T.; Nevalainen, T. Chiral 1,3,4-Oxadiazol-2-Ones as Highly Selective FAAH Inhibitors. *J Med Chem* **2013**, *56* (21), 8484–8496. https://doi.org/10.1021/jm400923s.

(30) Aaltonen, N.; Savinainen, J. R.; Ribas, C. R.; Rönkkö, J.; Kuusisto, A.; Korhonen, J.; Navia-Paldanius, D.; Häyrinen, J.; Takabe, P.; Käsnänen, H.; Pantsar, T.; Laitinen, T.; Lehtonen, M.; Pasonen-Seppänen, S.; Poso, A.; Nevalainen, T.; Laitinen, J. T. Piperazine and Piperidine Triazole Ureas as Ultrapotent and Highly Selective Inhibitors of Monoacylglycerol Lipase. *Chem Biol* **2013**, *20* (3), 379–390. https://doi.org/10.1016/j.chembiol.2013.01.012.

(31) Howlett, A. C.; Abood, M. E. CB1 and CB2 Receptor Pharmacology. In *Advances in Pharmacology*; Academic Press Inc., **2017**; Vol. 80, pp 169–206. https://doi.org/10.1016/bs.apha.2017.03.007.

(32) Jiang, L. I.; Collins, J.; Davis, R.; Lin, K. M.; DeCamp, D.; Roach, T.; Hsueh, R.; Rebres, R. A.; Ross, E. M.; Taussig, R.; Fraser, I.; Sternweis, P. C. Use of a CAMP BRET Sensor to Characterize a Novel Regulation of CAMP by the Sphingosine 1-Phosphate/G13 Pathway. *Journal of Biological Chemistry* **2007**, *282* (14), 10576–10584. https://doi.org/10.1074/jbc.M609695200.

(33) Finlay, D. B.; Cawston, E. E.; Grimsey, N. L.; Hunter, M. R.; Korde, A.; Vemuri, V. K.; Makriyannis, A.; Glass, M. Gαs Signalling of the CB1 Receptor and the Influence of Receptor Number. *Br J Pharmacol* **2017**, *174* (15), 2545–2562. https://doi.org/10.1111/bph.13866.

(34) Cawston, E. E.; Redmond, W. J.; Breen, C. M.; Grimsey, N. L.; Connor, M.; Glass, M. Real-Time Characterization of Cannabinoid Receptor 1 (CB1) Allosteric Modulators Reveals Novel Mechanism of Action. *Br J Pharmacol* **2013**, *170* (4), 893–907. https://doi.org/10.1111/bph.12329.

(35) Oyagawa, C. R. M.; de la Harpe, S. M.; Saroz, Y.; Glass, M.; Vernall, A. J.; Grimsey, N. L. Cannabinoid Receptor 2 Signalling Bias Elicited by 2,4,6-Trisubstituted 1,3,5-Triazines . *Frontiers in Pharmacology* . **2018**, p 1202.

(36) *Swiss Institute of Bioinformatics, SwissADME*. http://www.swissadme.ch/ (accessed 2020-11-18).

(37) Ross, T. L.; Ermert, J.; Hocke, C.; Coenen, H. H. Nucleophilic 18F-Fluorination of Heteroaromatic Iodonium Salts with No-Carrier-Added [18F]Fluoride. *J Am Chem Soc* **2007**, *129* (25), 8018–8025. https://doi.org/10.1021/ja066850h.

(38) Liang, S. H.; Wang, L.; Stephenson, N. A.; Rotstein, B. H.; Vasdev, N. Facile 18 F Labeling of Non-Activated Arenes via a Spirocyclic Iodonium(III) Ylide Method and Its Application in the Synthesis of the MGluR 5 PET Radiopharmaceutical [18 F]FPEB. *Nat Protoc* **2019**, *14* (5), 1530–1545. https://doi.org/10.1038/s41596-019-0149-3.

(39) Mu, L.; Fischer, C. R.; Holland, J. P.; Becaud, J.; Schubiger, P. A.; Schibli, R.; Ametamey, S. M.; Graham, K.; Stellfeld, T.; Dinkelborg, L. M.; Lehmann, L. 18F-Radiolabeling of Aromatic Compounds Using Triarylsulfonium Salts. *European J Org Chem* **2012**, *2012* (5), 889–892. https://doi.org/10.1002/ejoc.201101730.

(40) Gendron, T.; Sander, K.; Cybulska, K.; Benhamou, L.; Sin, P. K. B.; Khan, A.; Wood, M.; Porter, M. J.; Årstad, E. Ring-Closing Synthesis of Dibenzothiophene Sulfonium Salts and Their Use as Leaving Groups for Aromatic 18F-Fluorination. *J Am Chem Soc* **2018**, *140* (35), 11125–11132. https://doi.org/10.1021/jacs.8b06730.

(41) Preshlock, S.; Tredwell, M.; Gouverneur, V. ^{18} F-Labeling of Arenes and Heteroarenes for Applications in Positron Emission Tomography. *Chem Rev* **2016**, *116* (2), 719–766. https://doi.org/10.1021/acs.chemrev.5b00493.

(42) Sharninghausen, L. S.; Brooks, A. F.; Winton, W. P.; Makaravage, K. J.; Scott, P. J. H.; Sanford, M. S. NHC-Copper Mediated Ligand-Directed Radiofluorination of Aryl Halides. *J Am Chem Soc* **2020**, *142* (16), 7362–7367. https://doi.org/10.1021/jacs.0c02637.

(43) Tredwell, M.; Preshlock, S. M.; Taylor, N. J.; Gruber, S.; Huiban, M.; Passchier, J.; Mercier, J.; Génicot, C.; Gouverneur, V. A General Copper-Mediated Nucleophilic ^{18} F Fluorination of Arenes. *Angewandte Chemie International Edition* **2014**, *53* (30), 7751–7755. https://doi.org/10.1002/anie.201404436.

(44) Mossine, A. V.; Brooks, A. F.; Makaravage, K. J.; Miller, J. M.; Ichiishi, N.; Sanford, M. S.; Scott, P. J. H. Synthesis of [^{18} F]Arenes via the Copper-Mediated [^{18} F]Fluorination of Boronic Acids. *Org Lett* **2015**, *17* (23), 5780–5783. https://doi.org/10.1021/acs.orglett.5b02875.

(45) Zischler, J.; Kolks, N.; Modemann, D.; Neumaier, B.; Zlatopolskiy, B. D. Alcohol-Enhanced Cu-Mediated Radiofluorination. *Chemistry - A European Journal* **2017**, *23* (14), 3251–3256. https://doi.org/10.1002/chem.201604633.

(46) Bernard-Gauthier, V.; Mossine, A. V.; Mahringer, A.; Aliaga, A.; Bailey, J. J.; Shao, X.; Stauff, J.; Arteaga, J.; Sherman, P.; Grand'Maison, M.; Rochon, P. L.; Wängler, B.; Wängler, C.; Bartenstein, P.; Kostikov, A.; Kaplan, D. R.; Fricker, G.; Rosa-Neto, P.; Scott, P. J. H.; Schirrmacher, R. Identification of [18 F]TRACK, a Fluorine-18-Labeled Tropomyosin Receptor Kinase (Trk) Inhibitor for PET Imaging. *J Med Chem* **2018**, *61* (4), 1737–1743. https://doi.org/10.1021/acs.jmedchem.7b01607.

(47) Qiao, Z.; Mardon, K.; Stimson, D. H. R.; Migotto, M. anne; Reutens, D. C.; Bhalla, R. Synthesis and Evaluation of 6-[18F]Fluoro-3-(Pyridin-3-Yl)-1H-Indole as Potential PET Tracer for Targeting Tryptophan 2, 3-Dioxygenase (TDO). *Nucl Med Biol* **2020**, *84–85*, 1–10. https://doi.org/10.1016/j.nucmedbio.2019.12.007.

(48) Wang, L.; Mori, W.; Cheng, R.; Yui, J.; Hatori, A.; Ma, L.; Zhang, Y.; Rotstein, B. H.; Fujinaga, M.; Shimoda, Y.; Yamasaki, T.; Xie, L.; Nagai, Y.; Minamimoto, T.; Higuchi, M.; Vasdev, N.; Zhang, M. R.; Liang, S. H. Synthesis and Preclinical Evaluation of Sulfonamidobased [11C-Carbonyl]-Carbamates and Ureas for Imaging Monoacylglycerol Lipase. *Theranostics* **2016**, *6* (8), 1145–1159. https://doi.org/10.7150/thno.15257.

(49) Ahamed, M.; Attili, B.; van Veghel, D.; Ooms, M.; Berben, P.; Celen, S.; Koole, M.; Declercq, L.; Savinainen, J. R.; Laitinen, J. T.; Verbruggen, A.; Bormans, G. Synthesis and Preclinical Evaluation of [11C]MA-PB-1 for in Vivo Imaging of Brain Monoacylglycerol Lipase (MAGL). *Eur J Med Chem* **2017**, *136*, 104–113. https://doi.org/10.1016/j.ejmech.2017.04.066.

(50) Thomas, G.; Betters, J. L.; Lord, C. C.; Brown, A. L.; Marshall, S.; Ferguson, D.; Sawyer, J.; Davis, M. A.; Melchior, J. T.; Blume, L. C.; Howlett, A. C.; Ivanova, P. T.; Milne, S. B.; Myers, D. S.; Mrak, I.; Leber, V.; Heier, C.; Taschler, U.; Blankman, J. L.; Cravatt, B. F.; Lee, R. G.; Crooke, R. M.; Graham, M. J.; Zimmermann, R.; Brown, H. A.; Brown, J. M. The Serine Hydrolase ABHD6 Is a Critical Regulator of the Metabolic Syndrome. https://doi.org/10.1016/j.celrep.2013.08.047.

(51) Attili, B.; Celen, S.; Ahamed, M.; Koole, M.; Haute, C. van den; Vanduffel, W.; Bormans, G. Preclinical Evaluation of [18 F]MA3: A CB 2 Receptor Agonist Radiotracer for PET. *Br J Pharmacol* **2019**, *176* (10), 1481–1491. https://doi.org/10.1111/bph.14564.

(52) Imaizumi, M.; Briard, E.; Zoghbi, S. S.; Gourley, J. P.; Hong, J.; Fujimura, Y.; Pike, V. W.; Innis, R. B.; Fujita, M. Brain and Whole-Body Imaging in Nonhuman Primates of [11C]PBR28, a Promising PET Radioligand for Peripheral Benzodiazepine Receptors. *Neuroimage* **2008**, *39* (3), 1289–1298. https://doi.org/10.1016/j.neuroimage.2007.09.063.

(53) Leishman, E.; Cornett, B.; Spork, K.; Straiker, A.; MacKie, K.; Bradshaw, H. B. Broad Impact of Deleting Endogenous Cannabinoid Hydrolyzing Enzymes and the CB1 Cannabinoid Receptor on the Endogenous Cannabinoid-Related Lipidome in Eight Regions of the Mouse Brain. *Pharmacol Res* **2016**, *110*, 159–172. https://doi.org/10.1016/j.phrs.2016.04.020.

(54) Li, W.; Blankman, J. L.; Cravatt, B. F. A Functional Proteomic Strategy to Discover Inhibitors for Uncharacterized Hydrolases. *J. AM. CHEM. SOC* **2007**, *129*, 9594–9595. https://doi.org/10.1021/ja073650c.

(55) *High Resolution Image Viewer :: Allen Brain Atlas: Mouse Brain*. https://mouse.brain-map.org/experiment/siv?id=74047923&imageId=74056451&initImage=expression&contrast=0.5,0.5,0,255,4 (accessed 2020-11-18).

(56) Soethoudt, M.; Grether, U.; Fingerle, J.; Grim, T. W.; Fezza, F.; De Petrocellis, L.; Ullmer, C.; Rothenhäusler, B.; Perret, C.; Van Gils, N.; Finlay, D.; Macdonald, C.; Chicca, A.; Gens, M. D.; Stuart, J.; De Vries, H.; Mastrangelo, N.; Xia, L.; Alachouzos, G.; Baggelaar, M. P.; Martella, A.; Mock, E. D.; Deng, H.; Heitman, L. H.; Connor, M.; Di Marzo, V.; Gertsch, J.; Lichtman, A. H.; Maccarrone, M.; Pacher, P.; Glass, M.; Van Der Stelt, M. Cannabinoid CB2 Receptor Ligand Profiling Reveals Biased Signalling and Off-Target Activity. *Nat Commun* **2017**, *8* (1), 1–14. https://doi.org/10.1038/ncomms13958.

(57) Oyagawa, C. R. M.; de la Harpe, S. M.; Saroz, Y.; Glass, M.; Vernall, A. J.; Grimsey, N. L. Cannabinoid Receptor 2 Signalling Bias Elicited by 2,4,6-Trisubstituted 1,3,5-Triazines. *Front Pharmacol* **2018**, *9* (NOV), 1202. https://doi.org/10.3389/fphar.2018.01202.

(58) Finlay, D. B.; Cawston, E. E.; Grimsey, N. L.; Hunter, M. R.; Korde, A.; Vemuri, V. K.; Makriyannis, A.; Glass, M. Gαs Signalling of the CB1 Receptor and the Influence of Receptor Number. *Br J Pharmacol* **2017**, *174* (15), 2545–2562. https://doi.org/10.1111/bph.13866.

(59) Cawston, E. E.; Redmond, W. J.; Breen, C. M.; Grimsey, N. L.; Connor, M.; Glass, M. Real-Time Characterization of Cannabinoid Receptor 1 (CB1) Allosteric Modulators Reveals Novel Mechanism of Action. *Br J Pharmacol* **2013**, *170* (4), 893–907. https://doi.org/10.1111/bph.12329.

(60) Jung, B.; Taylor, P. A.; Seidlitz, J.; Sponheim, C.; Perkins, P.; Ungerleider, L. G.; Glen, D.; Messinger, A. A Comprehensive Macaque FMRI Pipeline and Hierarchical Atlas. *Neuroimage* **2021**, *235*, 117997. https://doi.org/10.1016/J.NEUROIMAGE.2021.117997.